Cerium dioxide nanoparticles coated with benzo[a]pyrene modify aryl hydrocarbon receptor activity, trophoblast differentiation and mitochondrial network phenotype in human placenta

Séverine A Degrelle, Gaëlle Deval, Arnaud Tête, Claire Mikolajczak, Frank Giton, Marie-Léone Vignaud, Sonja Boland, Céline J Guigon, Xavier Coumoul, Amal Zerrad-Saadi, et al.

Particle and Fibre Toxicology

RESEARCH

Open Access

Cerium dioxide nanoparticles coated with benzo[a]pyrene modify aryl hydrocarbon receptor activity, trophoblast differentiation and mitochondrial network phenotype in human placenta

Séverine A. Degrelle[1,2†], Gaëlle Deval[1†], Arnaud Tête[3], Claire Mikolajczak[1], Frank Giton[4], Marie-Léone Vignaud[1], Sonja Boland[5], Céline J. Guigon[1], Xavier Coumoul[3], Amal Zerrad-Saadi[1], Marie-Pierre Golinelli-Cohen[6], Thierry Fournier[1] and Ioana Ferecatu[1*]

Abstract

A growing body of epidemiological evidence links maternal exposure to air pollution with an increased risk of adverse pregnancy outcomes, such as preterm birth and low birth weight. Cerium dioxide nanoparticles (CeO_2 NPs or nanoceria) are emerging pollutants, used as additives in diesel fuels and cigarettes for their catalytic properties, and released into the environment. Due to their high surface-to-volume ratio and reactivity, CeO_2 NPs develop a surface coating during combustion, which may incorporate other released fuel-borne chemicals, such as benzo[a]pyrene (BaP), a known carcinogen, mutagen and reprotoxicant, raising concerns about their combined impacts on human health. To better reflect environmental reality, we produced BaP-coated CeO_2 NPs and exposed primary human trophoblasts and chorionic villi. Our findings show that BaP-coated CeO_2 NPs activate the aryl hydrocarbon receptor (AhR) pathway, enhancing trophoblast differentiation and syncytium formation, with effects distinct from those of BaP or CeO_2 NPs alone, or their unbound mixture. Additionally, exposure to CeO_2 NPs alone altered homeostasis of mitochondria, affecting their phenotype and function. While individual exposures or BaP-coated CeO_2 NPs had no detectable impact, parallel co-exposure resulted in a slight but significant reduction in basal respiration. Finally, uncoated CeO_2 NPs altered placental steroidogenesis, increasing estrone level while decreasing dehydroepiandrosterone level, with sex-specific effects. These findings suggest that CeO_2 NPs can influence the biological effects of BaP in the human placenta, including modulating trophoblast differentiation, as well as disrupting mitochondria homeostasis and steroid production, with potential implications for pregnancy outcomes in polluted environments.

Keywords BaP, Nanocerium, AhR, XRE, Steroidogenesis, Mitochondria, Human placenta, Cytotrophoblast, Syncytiotrophoblast, Lipid rafts

†Séverine A. Degrelle and Gaëlle Deval contributed equally to this work.

*Correspondence:
Ioana Ferecatu
ioana.ferecatu@u-paris.fr
Full list of author information is available at the end of the article

Background

The human placenta is a unique transitory organ, structurally complex and metabolically active. It is responsible for supplying the fetus with oxygen and nutrients, for endocrine function, waste evacuation, and also for protecting the fetus against harmful substances. The chorionic villus represents the structural and functional unit of the human placenta. It consists of a stromal core surrounded by trophoblasts, within which fetal vessels are enclosed [1]. The outer syncytiotrophoblast (ST) layer, a multinucleated syncytium, forms the epithelial covering of the villous tree, fed during early-to mid-gestation by an underlying pool of proliferative mononuclear villous cytotrophoblasts (VCT) that differentiate and fuse to renew the syncytium; his VCT layer gradually thins toward term, thereby diminishing the path between maternal blood and fetal vessels. The ST is in direct contact with the maternal blood by the apical microvillous membrane and is the seat of placental functions, ensuring the synthesis and the secretion of a wide range of hormones such as steroids, glycoproteins and angiogenic factors [2, 3]. The ST is also a selective barrier that protects the fetus against xenobiotics, although many substances can cross the placenta by different mechanisms [4, 5].

The VCT differentiation into ST is accompanied by major changes not only in cell morphology: for example, organelles like mitochondria also undergo deep structural and functional modifications [6]. Mitochondria play a major role in the regulation of cell metabolism, redox state, hormone production and apoptosis, which are critical for placental functions and successful fetal development. VCT mitochondria are relatively large, exhibiting a classic morphology with a lamellar crista structure characteristic of aerobic metabolism. The primary function of VCT mitochondria is the production of ATP by the respiratory chain. During syncytialization, the mitochondrial network undergoes extensive fragmentation, resulting in atypical small mitochondria with spherical morphology and a remodeled cristae structure. The ST mitochondrial matrix becomes less dense under transmission electron microscopy (TEM) [7]. These morphological changes are correlated with modifications in mitochondrial function, enabling the syncytium to acquire steroidogenic activity essential for progesterone (P4) production [8, 9]. Mitochondrial reshaping is ensured by a delicate balance between the two opposite processes called fusion and fission [9] that are regulated by a complex machinery of dedicated proteins [6].

Pollutants such as polycyclic aromatic hydrocarbons (PAH) and nanoparticles (NPs), particles with all three dimensions smaller than 100 nm) are widespread environmental contaminants. NPs exhibit a number of unique physicochemical properties that make them very attractive to industry; as a consequence, the list of consumer products containing manufactured nanomaterials is now rapidly expanding. Because of their high catalytic properties, CeO_2 NPs are added to gasoline to facilitate the regeneration of particulate filters, which are used to reduce particulate matter emissions, and thus increase fuel efficiency. Since the 2000 s, cerium dioxide (CeO_2) NPs (nanoceria, hereafter CeO_2 NPs), have been systematically added to diesel fuels (e.g. EnvirOx) to increase the efficiency of soot combustion. Consequently, CeO_2 NPs are now released into the environment from cars [10, 11], with a cerium (Ce) content increased by 6.5% [12]. Their applications have expanded due to their catalytic properties——such as in self-cleaning ovens and as additives in cigarettes [13]——as well as their use in glass polishing and UV-protection sunscreens where they serve as a substitute for titanium dioxide [14]. Due to the peculiar dual oxidation state of cerium (Ce^{3+} and Ce^{4+}) [15], which gives them pro- and antioxidant properties, CeO_2 NPs have also been proposed for various biomedical applications [16]. Due to their increased use and consequent exposure, CeO_2 NPs have gained the attention of the scientific community, which is now questioning their potential health effects. In addition, cerium has been detected in maternal blood at levels up to 5.18 ng/mL [17].

However, humans are rarely exposed to CeO_2 NPs alone, as they are typically found in combination with other pollutants from common emission sources. Due to their high surface-to-volume ratio and reactivity, CeO_2 NPs acquire a surface coating during the combustion of diesel fuels and cigarettes. This coating may consist of other released fuel-borne chemicals, such as benzo[a]pyrene (BaP) whose emissions increase by 35% in cerium-additive fuels [11, 18].

BaP is one of the most ubiquitous pollutants in ambient air and food, generated by the incomplete combustion of organic materials, including motor vehicle exhaust, residential heating, high-temperature cooking, and cigarette smoking. BaP is a five-ring benzene compound classified by the International Agency for Research on Cancer (IARC) as a Group I carcinogen (carcinogenic, mutagenic and reprotoxic agent for humans) and is also recognized as an endocrine disruptor [19]. BaP is considered a prototype PAH and, like tetrachlorodibenzo-p-dioxin (TCDD), has been widely used to assess the carcinogenic risk of particulate matters (PM) containing adsorbed PAH, including ultrafine particles (UFP) (particles smaller than 100 nm). The molecular basis of BaP toxicity is directly linked to the activation of the aryl hydrocarbon receptor (AhR), a ligand-activated transcription factor involved in xenobiotic detoxification. AhR activation allows the metabolic breakdown and elimination of many chemicals;

however for certain compounds like BaP, it also contributes to cellular toxicity through metabolic bioactivation (see below the roles of CYP450) [20]. Upon ligand-binding, AhR undergoes heterodimerization with the AhR nuclear translocator (ARNT) and binds to specific xenobiotic response elements (XRE) in the promoters of its target genes initiating gene transcription. Among AhR target genes are those encoding phase I xenobiotic metabolizing enzymes (XME), such as the microsomal cytochrome 450-dependent monooxygenases (CYP450 family), including CYP1A1, CYP1A2, and CYP1B1. CYP450 enzymes metabolize BaP into bioactive compounds, such as benzo[a]pyrene diol epoxide (BPDE), which can form DNA adducts, thereby contributing to the carcinogenic potential of BaP. Hence, CeO_2 NPs and BaP are often encountered together in the environment, making human exposure to their mixture a more realistic scenario.

Until now, few studies have addressed the adverse consequences of women's exposure to CeO_2 NPs during the sensitive window of human pregnancy [21, 22], and even fewer have explored the effects of the co-exposures with other pollutants, such as BaP [23]. The CeO_2 NPs used here, including their stable BaP surface coating at two environmentally relevant loading ratios, were synthesized and fully validated previously [24]. The first, referred to as low ratio (LR), reflects the environmental PAH/UFP ratio found in Parisian air pollution [25], which ranges from 0.15 to 2 mg of PAH per g of UFP and was adjusted to 1.66 mg BaP/g CeO_2 NPs. The second, four times higher (6.63 mg BaP/g CeO_2 NPs), is designated as high ratio (HR). Using XRE-plasmids previously described by our team [26], we assessed here AhR activity (indicative of BaP metabolization and bioactivation capacity), cytotrophoblast differentiation, mitochondrial morphology and function, as well as toxicant uptake in human placental models at term pregnancy. We compared the effects of BaP-coated CeO_2 NPs to individual exposures to each pollutant and to co-exposures (simultaneous addition of both pollutants separately). At non-cytotoxic concentrations, distinct effects were observed on AhR activity, trophoblast differentiation capacity and mitochondria morphology depending on exposure conditions. Moreover, we demonstrated that BaP-coated CeO_2 NPs are internalized into trophoblasts via lipid rafts.

Methods

Reagents

BaP (#31,306), AhR inhibitor (CH223191, #182,705), cyclohexane (CHX, #28,920), methyl-β cyclodextrin (MβCD, #C4555), sucrose (#S0389), staurosporine (Stau #S5921) and zirconium dioxide nanoparticles (ZrO_2 NPs, #643,122) were from Sigma-Aldrich. CeO_2 NPs were obtained from the Joint Research Centre of the European Union (NM-212, IHCP, Ispra, Italy).

Coating of CeO_2NPs with benzo[a]pyrene and preparation of suspensions

The detailed stable BaP-coating protocol and comprehensive physicochemical characterization including primary size (TEM), hydrodynamic diameter and polydispersity (DLS), Zeta-potential in relevant media, BaP surface loading, coating confirmation (attenuated total reflectance fourier-transform infrared (ATR-FTIR) and reverse phase-high pressure liquid chromatography (RP-HPLC)), and stability of the CeO_2 NPs batches employed have been previously published in detail [21, 24]; the most relevant parameters are summarized below for clarity.

Bare CeO_2 nanoparticles (NM-212, IHCP, Ispra, Italy) according to repository report JRC89825 have a polyhedral core of 28.4 ± 10 nm, a Brunauer–Emmett–Teller (BET) surface area of 27.2 m^2/g and a Zeta-potential of −23.4 mV in DMEM, agglomerating to ~ 380–500 nm in serum-containing medium [21]; whereas the same batch stably coated with benzo[a]pyrene retains the 10–100 nm core, yielding hydrodynamic diameters (DLS) of ~ 180–370 nm in placental medium, with the majority of the BaP remaining bound after 48 h in culture medium. The full dataset can be found in [24].

Two ratios of CeO_2 NPs coated with BaP were made for the treatments:

- A first ratio called the "Coating LR" approximating the PAH/UFP ratio found in Parisian atmospheric pollution [25] (0.15 to 2 mg PAH/g UFP converted to 1.66 mg BaP/g CeO_2 NPs, corresponding to 0.25 µM BaP per 10 $µg/cm^2$ CeO_2 NPs if all BaP is desorbed);
- A second ratio, called the "Coating HR" equivalent to 6.63 mg BaP/g CeO_2 NPs, corresponding to 1 µM BaP per 10 $µg/cm^2$ CeO_2 NPs if all BaP is desorbed. This ratio is four times higher than the low ratio and simulates a higher exposure scenario while remaining below the amount needed to form a complete monolayer of BaP around CeO_2 NPs (which would be 14.5 mg BaP/g CeO_2 NPs).

The weighed powdered CeO_2 NPs were suspended in glass tubes with CHX containing the desired quantity of BaP (Sigma-Aldrich #31,306) depending on whether the HR or LR coating was achieved. After homogenization by stirring on a vortex mixer at high intensity for one minute, the CeO_2 NPs solutions were distributed homogeneously into 2 mL glass tubes so that each tube contained 3 mg of CeO_2 NPs. The solutions were kept under a fume cupboard for 24 h to allow the CHX to completely evaporate. The tubes were then sealed with sterilized plastic

caps. CeO_2 NPs were also suspended in CHX without BaP (Sigma-Aldrich #227,048) and CHX was subsequently evaporated.

CeO_2 NPs, and BaP-coated CeO_2 NPs at low and high ratios were diluted in culture medium supplemented with 10% fetal calf serum (FCS, Eurobio #CVFSVF00-01, Les Ulis, France) at a concentration of 3 mg/mL and sonicated at 70% amplitude on ice, for 2 min with a cup horn (450 W and 50/60 Hz, Branson, Danbury, CT, USA).

Cell cultures, magnetofection and treatments

Placental tissues were obtained with the patients' written informed consent from non-smoking women with uncomplicated pregnancies who underwent normal cesarean sections at the maternity units at the Diaconesses Croix Saint-Simon (75,012 Paris, France), at Antony Private Hospital (92,160 Antony, France), and Institut Mutualiste Montsouris (75,014 Paris, France). This study was conducted in accordance with the Declaration of Helsinki and was approved by the local ethics committee (CPP 2015-mai-13909).

VCT were isolated from human term placentas as previously described [23, 24, 27–32]. Cells were seeded for nanoluciferase assays (XRE-pNL1.3 transfection) into either a sterile 12-well plate (500,000 cells/well, Corning #3512) or into a sterile 12-well removable chamber placed on cell culture–treated plastic slides (80,000 cells/well, Ibidi #81,201) for fluorescence experiments (immunofluorescence and XRE-H2B-eGFP transfection).

To study the activity of AhR transcription factor after exposure of trophoblasts to these pollutants, we used two XRE-reporter vectors previously described by our team [26] (XRE-pNL1.3[secNLuc] and XRE-H2B-eGFP). VCT transfection with XRE-pNL1.3[secNluc] allows monitoring of the kinetics of reporter gene activation by measuring the luciferase directly secreted into cell media over time without harming the cells. This process was carried out as described in [30, 33]. Briefly, the transfection complexes were composed of Opti-MEM medium mixed with Lipofectamine 2000 CD (Invitrogen), Magnetofection CombiMag (OZ Biosciences), and XRE-pNL1.3[secNLuc] (Addgene Plasmid #182,294) or empty-pNL1.3 (Promega Corporation, JQ437372)/CMV-ss.mCherry (constructed as described in [33]) for nanoluciferase assays or XRE-H2B-GFP (Addgene Plasmid #182,295) and CMV-H2B-mScarlet-I (Addgene Plasmid #182,297) for immunofluorescence. Following 20-min incubation at room temperature, the mixture was distributed into the wells (75 µL/well in the 12-well plate, 30 µL/well in the 12-well slide). Prior to VCT seeding, culture plates and slides were incubated on a magnetic plate (OZ Biosciences) at 37 °C and 5% CO_2 for at least 10 min. The assembly was then transferred back into the incubator. After overnight incubation, transfected cells were washed and treated for 24 h with 10 µg/cm^2 CeO_2 NPs, 10 µg/cm^2 CeO_2 NPs coated with 2 concentrations of BaP (0.25 or 1 µM), 10 µg/cm^2 CeO_2 NPs co-exposed with 2 concentrations of BaP (0.25 or 1 µM), 2 concentrations of BaP only (0.25 or 1 µM), 2"vehicle"controls due to BaP dilution in CHX (0.06 and 0.25%) or 3 µM of AhR antagonist (CH223191) as control.

Nanoluciferase assay

Cells transfected with XRE-pNL1.3[secNLuc] or empty-pNL1.3/CMV-ss.mCherry were cultured in a 24-well plate for 24 h at 37 °C. Then, cells were treated for 48 h with 10 µg/cm^2 NPs, 10 µg/cm^2 NPs coated with 2 concentrations of BaP (0.25 or 1 µM), 10 µg/cm^2 NPs co-exposed with 2 concentrations of BaP (0.25 or 1 µM), 2 concentrations of BaP only (0.25 or 1 µM), 2"vehicle"controls due to BaP dilution in CHX (0.06 and 0.25%) or 3 µM of AhR antagonist (CH223191) as control. Supernatants (75 µL) collected at 24 h and 48 h were dispensed in duplicate into the wells of a 96-well plate (#3610, Corning). NanoLuc® luciferase activity in supernatants was quantified using the Nano-Glo® Luciferase Assay (#N1130 Promega Corporation), according to the manufacturer's instructions. Measurements of luminescence and mCherry fluorescence (Ex: 587 nm, Em: 610 nm) were performed in each well using an EnSpire Multimode plate reader (Perkin Elmer). Luciferase luminescence reading were first normalized to the corresponding mCherry signal, and then to the values obtained from cells transfected with the empty-pNL1.3.

Immunofluorescence and image analysis

Cells cultured and treated in a 12-well removable chamber were fixed in 4% PFA for 20 min at room temperature, washed and stored at 4 °C in PBS.

For the fusion index assay, cells were permeabilized in 0.5% Triton X-100 in PBS for 30 min, and then incubated for 1 h at 37 °C with 2 µg/mL GATA3 (#sc-268, Santa Cruz) and 2 µg/mL β-catenin (CTNNB #51,067–2-AP, Proteintech) or 1 µg/mL desmoplakin (DSP, (#ab71690, Abcam) primary antibodies in blocking solution, as described in [32–34]. Following three washes with 0.1% Tween-20 in PBS (PBST), cells were incubated with the VectaFluor™ Excel R.T.U. Antibody Kit containing DyLight® 594 anti-mouse IgG antibody (#DK-1488, Vector Laboratories), according to the manufacturer's instructions. After an additional three washes with PBST, cells were incubated for 1 h at room temperature in the dark with Alexa Fluor® 488 Donkey anti-Rabbit IgG (H + L) Highly Cross-Adsorbed secondary antibody (#A21206, Invitrogen; 1:500 in PBST). Cells underwent three additional PBST washes, followed by

DAPI counterstaining for 10 min at room temperature. Finally, slides were mounted with Fluorescence Mounting Medium (#S3023, Dako) and stored at 4 °C.

For XRE-H2B-eGFP experiments, cells were blocked in 5% BSA (IgG-free) and 0.1% Tween-20 in PBS (PBST) for 30 min at room temperature, and then incubated for 1 h at 37 °C with 1 µg/mL DSP (#ab71690, Abcam) primary antibody in blocking solution, as described in [30, 33]. After three washes with 0.1% Tween-20 in PBS (PBST), cells were incubated in the dark at room temperature for 1 h with Alexa Fluor® 647 Donkey anti-Rabbit IgG (H + L) Highly Cross-Adsorbed secondary antibody (#A31573, Invitrogen; 1:500 in PBST), then washed three times in PBST. Finally, slides were mounted with Fluorescence Mounting Medium (#S3023, Dako) and stored at 4 °C.

For JC-1 experiments, cells were blocked in 1% BSA/0.05% saponin (IgG free) in CellCover for 1 h at room temperature and then incubated overnight at 4 °C with 1 µg/mL E-cadherin (#ab11512, Abcam) primary antibody in blocking solution. After three washes with 0.1% Tween-20 in CellCover, cells were incubated with Donkey anti-Rat IgG (H + L) Cross-Adsorbed DyLight® 650 secondary antibody (#SA510029, Invitrogen; 1:500 in 0.1% Tween-20/CellCover) for 1 h in the dark at room temperature, then washed three times with 0.1% Tween-20 in CellCover and counterstained with DAPI for 10 min at room temperature. Finally, cells were covered with CellCover and stored at 4 °C. Confocal microscopy images were acquired using a Leica SP8 inverted microscope fitted with Plan Apo × 40/1.3 and × 60/1.4 oil immersion objectives. Image processing was performed with ImageJ software (version 1.53q, National Institutes of Health, https://imagej.net/ij/). The fusion index was calculated in at least three placentas from seven non-overlapping images per replicate and determined as described in [34]: [100 − % (number of $GATA3^+$ nuclei/total number of DAPI nuclei)]. Quantification of XRE-H2B-eGFP was performed as described in [31]. In summary, a minimum of 50 nuclei per condition were examined across three independent experiments. For signal quantification, fluorescence intensity was integrated over the whole nuclear area.

Mitochondrial network analysis and stimulated emission depletion (STED) imaging

Cells cultured and treated in an 8-well chamber were fixed in 4% PFA/0.2% glutaraldehyde in PHEM buffer (68 mM PIPES, 25 mM HEPES, 15 mM EGTA, 3 mM $MgCl_2$) for 20 min at 37 °C for mitochondrial morphology, and washed and stored at 4 °C in PBS. Cells were first permeabilized in 0.1% Triton X-100 in PBS for 7 min, then blocked in 5% SAB in PBS for 1 h at room temperature and then incubated for 1 h at 37 °C with anti-COX2 (1:1000) primary antibody in blocking solution. After three washes with 0.1% Tween-20 in PBS (PBST), cells were incubated in the dark at room temperature for 1 h with Goat Anti-Rabbit-IgG—Atto 550 (H + L) (43,328-1ML-F, Sigma; 1:800 in PBST), washed three additional times in PBST and then counterstained with DAPI for 10 min at room temperature. Slides were mounted with Fluorescence Mounting Medium (#S3023, Dako) and stored at 4 °C. COX2 antibody was generated by the group of Dr Anne Lombès, as previously reported [35].

STED images were obtained using a Leica TCS SP8 inverted microscope with a time-gated STED module (Leica Microsystems GmbH, Germany), equipped with a white light laser (WLL) and an HC PL APO CS2 100x/1.40 oil objective. The excitation wavelength was 558 nm, and depletion was achieved with a 660 nm laser. The pinhole was set to 0.5 Airy units, and the pixel size was optimized. Images of 1024 × 1024 pixels were acquired at a scan speed of 600 Hz with the number of line average equal to 16 and frame accumulation of 2. Signals were detected with a hybrid detection system (Leica HyD). To improve the signal-to-noise ratio, the images were deconvolved with Huygens Professional Software (Scientific Volume Imaging) using the fast deconvolution presetting. Mitochondrial quantification was performed by the Mitochondrial Analyzer plugin within ImageJ. The settings for thresholding were adjusted, with enhance local contrast turned off and settings for block size and C-value adapted per set of images, before analysis with default settings [36, 37]. For deconvolved images, a block size of 10 and C-value of 5 were used.

Protein extraction and western blot

Total protein extracts were prepared from trophoblast cells cultured in 60 mm dishes by lysing the cells in Ripa lysis buffer (Cell Signaling Technology #9806S), supplemented with protease inhibitors (1:100, Protease Inhibitor Cocktail Set I, Calbiochem Merck #539,131) and phosphatase inhibitors (1:50, Phosphatase Inhibitor Cocktail Set V, Calbiochem Merck # 524,629). Protein lysates were centrifuged at 14,000 × g for 5 min, and the supernatants were stored at − 80°C. Protein concentrations were measured using the Pierce™ BCA Protein Assay Kit (Thermo Fisher Scientific #23,235). Equal amounts of proteins (30 µg) were resolved by SDS-PAGE using either 7.5% or 4–15% mini-PROTEAN TGX

Table 1 Characteristics of the primers used

Genes		Primer sequences	Efficiency	T_m(°C)	Bases GC (%)	Fragment length (bp)
MFN1	F	5′-AGG-AAC-TGA-TGG-AGA-TAA-AGC-C-3′	2	57.57	45	139
	R	5′-CCA-AAA-CAC-ACG-TAC-AAG-ACA-G-3′		58.06	45	
MFN2	F	5′-ATC-CCC-ACT-TAA-GCA-CTT-TGT-C-3′	1,89	58.58	45	112
	R	5′-ATT-CCT-GTA-CGT-GTC-TTC-AAG-G-3′		58.07	45	
OPA1	F	5′-TAA-CGA-GGG-AAA-GAG-AAA-CCT-G-3′	1,81	57.73	45	151
	R	5′-TTG-ACC-ATG-GAG-TAC-AAC-TGT-G-3′		58.26	45	
DRP1	F	5′-GGC-AAC-TGG-AGA-GGA-ATG-3′	1,99	54.99	56	108
	R	5′-GGC-ATG-ACC-TTT-TTG-TGG-3′		54.24	50	
PGC-1α	F	5′-ACC-ACT-CCT-CCT-CAT-AAA-GCC-3′	2	59.16	52	133
	R	5′-TGC-CTT-GTG-TAC-CAG-AAG-ACT-C-3′		59.96	50	
RPL13	F	5′-CTG-GCG-TGG-AAA-TAG-GTG-AT-3′	1,97	57.67	50	215
	R	5′-CGG-CCC-ACC-TTA-ACT-TTA-CA-3′		57.81	50	
RPLP0	F	5′-TCG-ACA-ATG-GCA-GCA-TCT-AC-3′	1,96	58.06	50	223
	R	5′-GCC-TTG-ACC-TTT-TCA-GCA-AG-3′		57.57	50	
SDHA	F	5′-TGG-GAA-CAA-CAG-GGC-ATC-TG-3′	1,99	60.28	55	86
	R	5′-CCA-CCA-CTG-CAT-CAA-ATT-CAT-G-3′		58.48	45	

precast gels (Bio-Rad #4,561,085 #4,561,084, Marnes- la-Coquette, France) under reducing conditions with 10% dithiothreitol (Sample Reducing Agent 10×, Invitrogen #NPs0009, Waltham, MA, USA). Proteins were then transferred onto a nitrocellulose membrane (Trans-blot Turbo Transfer pack, 0.2 µm nitrocellulose, Bio-Rad #1,704,159). Membranes were incubated at 4 °C overnight with the primary antibody, followed by 1-h incubation at room temperature with the appropriate DyLight 680 or 800 Fluor-conjugated secondary antibody (Thermo Fisher Scientific #35,568 and #35,521). The primary antibodies used were mouse anti-mitofusin 2 (1:1000, Abcam # ab56889), rabbit anti-mitofusin-1 (1:1000, Cell Signaling #14,739), rabbit anti-optic atrophy 1 (OPA1, 1:1000, Abcam #ab42364), rabbit anti-dynamin-related protein 1 (anti-DRP1, 1:1000, Cell Signaling #5391), rabbit anti-fission 1 (FIS1, 1:1000, Sigma-Aldrich #HPA017430), rabbit anti-voltage-dependent anion channel 1 (anti-VDAC1, 1:1000, Homemade), and mouse anti-vinculin (1:1000, Sigma-Aldrich #1V9131). The secondary antibodies used were DyLight 800-conjugated anti-mouse IgG (1:20,000, Thermo Fisher Scientific #35,521) or DyLight 680-conjugated anti-rabbit IgG (1:20,000, Thermo Fisher Scientific #35,568). Primary and secondary antibodies were diluted in the following dilution buffers according to the manufacturers'instructions: 1X TBS, 0.1% Tween-20, 5% nonfat dry milk, 0.1% sodium azide or 1X TBS, 0.1% Tween-20, 5% BSA (Jackson ImmunoResearch #001–000-173). Blots were scanned with an Odyssey Imaging System (Li-COR, Bad Homburg, Germany). Band intensity quantification was carried out using Odyssey software (Li-COR).

RNA extraction, reverse transcription and real-time quantitative PCR

The treated VCT were harvested using 0.05% trypsin–EDTA (Gibco #25,300,054). Total RNA was then isolated from cell pellets containing 3 million cells using the RNeasy mini kit (Qiagen #74,104), following the manufacturer's protocol, including on-column DNase-treatment (Qiagen #79,254). After RNA elution, the concentration (A260) and the purity (A260/A280 and A260/A230 ratios) of samples were assessed using a Nanodrop ND-1000 spectrophotometer. RNAs with an A260/A230 ratio of less than 1.6 were purified with the RNeasy MinElute Cleanup kit (Qiagen #74,204). The total RNAs recovered were stored at − 80 °C after addition of 1 µL of RNase-OUT (Invitrogen #10,777,019). Reverse transcription of 1 µg of RNA was carried out using the SuperScript™ III Reverse Transcriptase kit (Invitrogen #18,080,044), with random primer (Invitrogen #48,190,011). Quantitative RT-PCR (RT-qPCR) was performed in a total volume of 10 µL, comprising 10 ng of cDNA, 5 µM of each primer, and 5 µL of SYBR™ Green (Master Mix PowerTrack Applied Biosystems #A46111), using the CFX384 Real-Time PCR Detection System (Bio-Rad). All primers (Table 1) were provided by Eurogentec and validated beforehand. PCR cycling conditions included an initial polymerase activation step (2 min, 95 °C), followed by denaturation (15 s, 95 °C) and combined annealing/extension (1 min, 60 °C). A final melting curve analysis was performed to ensure no contamination. The threshold cycle (Ct) was measured as the number of cycles at which the fluorescence emission first exceeds the background. The 3 reference

genes used were ribosomal protein L13 (*RPL13)*, ribosomal protein L0 (*RPLP0)*, and succinate dehydrogenase complex flavoprotein subunit A *(SDHA)*. The relative amounts of mRNA were estimated using the Pfaffl method [38] to take into account the primer's efficiency and expressed as fold change:

$$\text{Ratio} = \frac{\left(E_{\text{target}}\right)^{\triangle \text{Ct target}}}{\text{Geometric mean}\left[(E_{\text{ref1}})^{\triangle \text{Ct ref1}};\ (E_{\text{ref2}})^{\triangle \text{Ct ref2}};\ (E_{\text{ref3}})^{\triangle \text{Ct ref3}}\right]}$$

JC-1 mitochondrial membrane potential

Mitochondrial membrane potential was assessed according to the manufacturer's protocol (#T3168, Invitrogen). Briefly, cells were plated overnight at 50,000 cells/well in triplicate in a 96-well plate and subsequently treated for 24 h and 48 h with 10 µg/cm^2 NPs, 10 µg/cm^2 NPs coated with 2 concentrations of BaP (0.25 or 1 µM), 10 µg/cm^2 NPs co-exposed with 2 concentrations of BaP (0.25 or 1 µM), 2 concentrations of BaP only (0.25 or 1 µM), 2"vehicle"controls due to BaP dilution in CHX (0.06 and 0.25%) or 3 µM of AhR antagonist (CH223191) as control. As a control, 1 µM Stau treatment was performed for 3 h. Then JC-1 dye-loading solution (1 µM final concentration) was added and incubated for 30 min. The fluorescent intensities for both aggregates (Ex: 570 nm, Em: 590 nm) and monomeric (Ex: 514 nm, Em: 530 nm) forms JC-1 were measured in each well at 37 °C using an EnSpire Multimode plate reader (Perkin Elmer). Then, cells were fixed with CellCover (Anacyte Laboratories) for confocal imaging.

Measurement of mitochondrial respiration by Seahorse

Agilent Seahorse XFe24 analyzer and XF Cell Mito Stress Test kits from Agilent (Santa Clara, CA) were used to assess the oxygen consumption rate (OCR). Cells were seeded on Seahorse XFe24 culture plates at a density of 100,000 cells/well for 16 h. Cells were washed with Hanks' balanced salt solution (HBSS) and incubated for 24 h with the different treatments: 10 µg/cm^2 CeO_2 NPs, 10 µg/cm^2 CeO_2 NPs coated with 2 concentrations of BaP (0.25 or 1 µM), 10 µg/cm^2 CeO_2 NPs co-exposed with 2 concentrations of BaP (0.25 or 1 µM), 2 concentrations of BaP only (0.25 or 1 µM), a control due to BaP dilution in CHX 0.25%, 3 µM of AhR antagonist (CH223191) and 3 µM of CH223191 with 10 µg/cm^2 CeO_2 NPs coated with BaP at 0.25 µM. Culture media were exchanged with Seahorse XF DMEM pH 7.4, supplemented with 10 mM glucose, 2 mM glutamine, and 1 mM pyruvate and cell culture microplates were placed in a 37 °C non-CO_2 incubator for one hour prior to assay. The sequential injections of selective electron transport chain (ETC) inhibitors and uncoupling agents included oligomycin (1.5 µM), FCCP (1 µM) and a mixture of rotenone and antimycin A (0.5 µM). Addition of oligomycin inhibits ATP synthase, resulting in a reduction of OCR, which is linked to mitochondrial ATP production. The addition of FCCP, an uncoupling agent, stimulates electron transport chain (ETC) activity and results in a maximum OCR. Addition of rotenone/antimycin A inhibits complexes I and III, respectively, leading to a shutdown of mitochondrial respiration. Mitochondrial spare capacity was calculated from the difference between basal OCR and FCCP-stimulated maximal OCR. The OCR values were normalized to the number of nuclei obtained after Hoechst staining and counted using an automated cell imaging system (ImageXpress Pico, Molecular Devices).

Quantification of steroids in VCT supernatants by GC–MS/MS

The supernatants of VCT were treated for 48 h with CeO_2 NPs at 10 µg/cm^2 and the untreated supernatants were stored for the quantification of steroids.

Dehydroepiandrosterone (DHEA), testosterone (T), dihydrotestosterone (DHT), estrone (E1), estradiol (E2), δ4-androstenedione (A4), P4, and 17 hydroxy-progesterone (17OHP) were measured by GC–MS/MS.

Briefly, each sample (VTC supernatants, calibration standards, quality controls, and blank matrix) was collected in a 4 mL borosilicate tube. A spiking solution of deuterated steroid internal standards (IS) (10 µL containing 1 ng of T-d8, 0.5 ng of DHT-d3, 100 pg of E1-d4, 50 pg of E2-d4, 2 ng of 4-dione-d7, and 3 ng of Prog-d9, except for blank matrix) (CDN Isotopes, Inc., Point-Claire, Canada), 2.8 mL of 1-chlorobutane was added to each sample. Following 2 min of vortexing and brief centrifugation, the upper organic phase was transferred onto a pre-conditioned Hypersep SI 500 mg SPE minicolumn (Thermo Scientific #60,108–315). The column was subsequently washed with 6 mL of ethyl acetate/hexane (1/9, v/v) to remove non-target compounds. The fraction containing the steroids of interest was then eluted using 4 mL of ethyl acetate/hexane (1/1, v/v) and evaporated to dryness at 60 °C.

DHEA, T, DHT, E1, and E2 were derivatized as previously described [39] with pentafluorobenzoyl chloride (Sigma-Aldrich #103,772). The final extracts were reconstituted in 20 µL of isooctane and transferred into conical vials for GC injection.

A4, P4, and 17OHP, were derivatized with 50 µL of heptafluorobutyric anhydride (Apollo Scientific #PC4470) and anhydrous acetone (1/1) mixture. The final extracts were reconstituted in 20 µL of anhydrous n-hexane, and transferred to conical vials for injection into the GC system (GC-2010 Plus, Shimadzu) equipped with a VF-17MS capillary column (50% phenylmethylpolysiloxane, Agilent Technologies). A TQ8050 triple quadrupole mass spectrometer (Shimadzu) equipped with a chemical ionization source (NCI), and operating in Q3 single ion monitoring (SIM) mode, was used for the detection of DHEA, DHT, T, E1, and E2, and with an electron impact source operating in multiple reaction monitoring (MRM) mode for the detection of A4, P4, and 17OHP.

For NCI detection, the reagent gas was methane, and the GC was performed in pulsed splitless mode with a 1-min pulsed splitless-time. The oven temperature was initially 150 °C for 0.50 min, further increased to 305 °C at 20 °C/min and held at 305 °C for 3.60 min, and then to 335 °C at 30 °C/min and held at 335 °C for 1.7 min. The injection port and transfer line temperatures were respectively 290 and 280 °C. The flow rate of helium (carrier gas) was kept constant at 0.96 mL/min. The mass spectrometer CI source temperature was 220 °C.

For EI detection, GC was performed in splitless mode with a 1-min splitless-time. The temperature in the oven was initially 70 °C for 1 min, further increased to 238 °C at 25 °C/min, and then to 261 °C at 5 °C/min. The injection port and transfer line temperatures were respectively 290 and 280 °C. The flow rate of carrier gas was kept constant at 0.70 mL/min. The mass spectrometer EI source was 230 °C.

Linearity of steroid quantification was assessed by plotting the ratio of the steroid peak area to that of internal standard against the corresponding steroid concentration for each calibration standard.

Accuracy, target ions, corresponding deuterated internal control, range of detection, low limit of quantification (LLOQ), and intra- inter-assay CVs of the quality control are reported in Supplemental Table S1.

Quantification of oxysterols in VCT supernatants

7α-Hydroxycholesterol (7aOHC), 7β-hydroxycholesterol (7bOHC), 5α,6α-epoxycholestanol (5a6a Echol), 5β,6β-epoxycholestanol (5b6b Echol), 25-hydroxycholesterol (25OHC), 7-ketocholesterol (7KChoL), and 4β-hydroxycholesterol (4bOHC) were measured by GC–MS/MS.

Each sample was collected in a screw-capped vial sealed with a Teflon septum, and 50 µL of spiking solution of deuterated oxysterol internal standards were added together with 20 ng of 7aOHC-d7, 7bOHC-d7, 5a6a Echol-d7, 5b6b Echol-d7, 25OHC-d6, 4bOHC-d7, and 7KChol-d7 (Avanti Research, Alabama, USA). To prevent auto oxidation, 20 µL of butylated hydroxytoluene (12.5 mg/mL of methanolic alcohol; Sigma-Aldrich #B1378), and 20 µL of EDTA (25 mg/mL of deionized water; Sigma-Aldrich #O3664) were added to each vial and flushed with nitrogen to remove air.

Alkaline hydrolysis was carried out at room temperature (21 °C) for 2 h in the presence of 180 µL of 5.9 M methanolic potassium hydroxide solution. Oxysterols were subsequently extracted using 2.8 mL of hexane. After vortexing for 2 min and brief centrifugation, the upper organic phase was loaded on a pre-conditioned Hypersep SI 500 mg SPE minicolumn (Thermo Scientific #60,108–315) using 6 mL of hexane. The column and adsorbed material were then washed with 2-propanol/hexane (3.5 mL; 5/95). The second fraction containing the compounds of interest was eluted with 2-propanol/hexane (4 mL; 3/7), then evaporated at 70 °C to dryness with nitrogen. Final extracts were reconstituted in methanol, then transferred into conical vials, evaporated under nitrogen at 70 °C to dryness, and converted into trimethylsilyl ethers with 20 µL of BSTFA (with 1% TMCS; Supelco #B-023), and 20 µL of anhydrous pyridine (VWR #83,684.230) for 30 min at 70 °C.

Evaporated final extracts were reconstituted in 30 µL of hexane for injection into the GC system (GC-2010 Plus, Shimadzu) using a 50% phenylmethylpolysiloxane VF-17MS capillary column (Agilent Technologies). A TQ8050 triple quadrupole mass spectrometer (Shimadzu) equipped with an electron impact source operating simultaneously in multiple reaction monitoring (MRM) and Q3 single ion monitoring (SIM) modes, was used in MRM mode for the detection of 7aOHC, 7bOHC, 4bOHC, 25OHC, and 7KChol, and in SIM mode for the detection of 5a6a Echol, and 5b6b Echol.

GC was performed in splitless mode with a 1-min splitless-time. The temperature in the oven was initially 180 °C for 0.5 min, further increased to 250 °C at 20 °C/min, and then to 300 °C for 3.2 min at 5 °C/min. The injection port and transfer line temperatures were respectively 280 and 270 °C. The flow rate of carrier gas was maintained constant at 0.80 mL/min. The mass spectrometer EI source was 250 °C.

Steroid quantification linearity was verified by plotting the ratio of the steroid peak area to that of the internal standard against the known concentrations of the calibration standards.

Accuracy, target ions, corresponding deuterated internal control, range of detection, low limit of quantification (LLOQ), and intra- inter-assay CVs of the quality control are reported in Supplemental Table S2.

CeO_2NPs uptake study

For explant cultures, chorionic villi from term placentas ($n=3$) were cultured in duplicate, placed in a 24-well plate precoated with 1% (w/v) agarose [40] and cultured in 2 mL of DMEM supplemented with 10% FCS, 2 mM glutamine, 100 IU/mL penicillin, and 100 µg/mL streptomycin. Explants were first pre-treated for 1 h with MβCD (10 mM) and sucrose (450 mM). The concentrations of these inhibitors were used according to previous reports [41]. Then, 10 µg/cm^2 of CeO_2 NPs coated with 1 µM BaP was added and incubated for 48 h. Placental explants were fixed with 4% PFA overnight at 4 °C, washed 3 times and stored in 1X PBS at 4 °C until use. Placental explants were permeabilized and blocked in 0.3% Triton X-100/1% BSA (IgG-free) in PBS (PBST) for 3 h at room temperature, and incubated overnight at 4 °C with 2 µg/ml Cytokeratin 7 (CK7, a trophoblast-specific marker, # SAB4501652, Sigma Aldrich), 1.5 µg/mL CD31 (an endothelial marker, # M0823, Dako) primary antibodies in 1% BSA (IgG-free)/0.05% saponin. The next day, explants were washed four times with PBST for 30 min, and incubated overnight at 4 °C with Alexa Fluor® 488 Donkey anti-Mouse and an Alexa Fluor® 555 Donkey anti-Rabbit IgG (H+L) Highly Cross-Adsorbed secondary antibodies (respectively, #A21202 and #A31572, Invitrogen; 1:500 in PBST), and nuclei were counterstained with SYTOX Deep Red (#S11380, Invitrogen; 1: 2,000). The following day, explants were washed four times with PBST for 30 min. Finally, slides were mounted with Fluoromount-G™ (#FP-483331, FluoProbes) and stored at 4 °C. Confocal imaging was performed using a Leica SP8 inverted microscope fitted with Plan Apo oil immersion objectives (×40/1.3 and ×60/1.4). Imaging processing was carried out with ImageJ software (version 1.53q, National Institutes of Health, https//imagej.nih.gov/ij/).

Statistics

All measurements were performed at least in three independent experiments. Statistical analyse were conducted using the GraphPad Prism 10 version 10.0.2 (GraphPad software, La Jolla, CA, USA). Data are presented as the mean ± standard error of mean (SEM). Data normality was assessed using the Shapiro–Wilk test. For normally distributed data, comparisons between groups were performed using parametric unpaired Student's *t*-tests or one-way ANOVA, followed by Dunnett's or Sidak's multiple comparison tests. For non-normally distributed data, the nonparametric Wilcoxon–Mann–Whitney test or Kruskal–Wallis test with Dunn's post-hoc analysis was applied. Differences were considered statistically significant at $p<0.05$ (*, #, §), $p<0.01$(**, ##, §§), $p<0.001$(***, ###, §§§), or $p<0.0001$(****, ####, §§§§).

Results

Effects of pollutants on AhR activity evaluated by XRE-mediated transcriptional activation of the reporter gene

In this study, VCT purified from term placenta were exposed either to coatings at LR and HR, co-exposures at LR and HR by simultaneous addition, or individually exposed to either CeO_2 NPs or BaP. AhR antagonist CH223191 was used to define the AhR baseline activity and CHX as solvent control (% relative to 0.25 µM for LR or to 1 µM BaP for HR). Results obtained with the XRE-pNL1.3[secNLuc] plasmid showed that the treatment with CeO_2 NPs alone significantly inhibited AhR activity in a similar way to that of the AhR antagonist after

(See figure on next page.)

Fig. 1 Effect of BaP-coated CeO_2 NPs on AhR activity using XRE-reporter gene plasmids. **A** After 16 h of culture, VCT co-transfected with XRE-pNL1.3[secNluc] and CMV-ss.mCherry plasmids were treated for 48 h with 10 µg/cm^2 CeO_2 NPs (CeO_2 NPs), 10 µg/cm^2 CeO_2 NPs coated with 2 concentrations of BaP (Coating LR at 0.25 µM and Coating HR at 1 µM), 10 µg/cm^2 CeO_2 NPs co-exposed with 2 concentrations of BaP (Co-exposure LR at 0.25 µM and Co-exposure HR at 1 µM), 2 concentrations of BaP alone (BaP LR at 0.25 µM and BaP HR at 1 µM), 2"vehicle"controls due to BaP dilution in cyclohexane (CHX 0.06 and 0.25%) or 3 µM of AhR antagonist (CH223191). AhR activity was determined using the Nano-Glo® Luciferase system (Promega). For each condition, 75 µL of culture media after 24 h or 48 h of treatment was analyzed in duplicate. Values are presented as mean ± SEM of fluorescence intensity normalized to (i) the mCherry signal corresponding to (ii) control cells transfected with the pNL1.3-empty plasmid and (iii) untreated cells ($n=6$ in duplicate). Statistical analysis was performed by means of one-way ANOVA Dunnett test against (i) untreated control; * $p<0.05$, ** $p<0.01$, *** $p<0.001$, **** $p<0.0001$, (ii) Coating LR; #### $p<0.0001$, (iii) Coating HR; §§ $p<0.01$, and the one-way ANOVA Sidak test to compare 24 h and 48 h; ▲▲ $p<0.01$. **B** After 16 h of culture, VCT co-transfected with XRE-H2B-GFP (green) and CMV-H2B-mSarlet plasmids (red) were treated for 24 h with 10 µg/cm^2 CeO_2 NPs (CeO_2 NPs), 10 µg/cm^2 CeO_2 NPs coated with 2 concentrations of BaP (Coating LR at 0.25 µM and Coating HR at 1 µM), 10 µg/cm^2 CeO_2 NPs co-exposed with 2 concentrations of BaP (Co-exposure LR at 0.25 µM and Co-exposure HR at 1 µM), 2 concentrations of BaP alone (BaP LR at 0.25 µM and BaP HR at 1 µM), 2"vehicle"controls due to BaP dilution in cyclohexane (CHX 0.06 and 0.25%) or 3 µM of AhR antagonist (CH223191). Representative images of cells fixed at 24 h and subjected to immunostaining with anti-desmoplakin antibody (DSP, magenta). Scale bar: 20 µm. AhR activity was assessed by quantification of XRE-H2B-eGFP fluorescence intensity (lower bar graph). Values are presented as the mean ± SEM of fluorescence intensity normalized to the untreated control ($n=3$ placentas, 3 non-overlapping images per replicate with > 50 nuclei). Statistical analysis was performed using Kruskal–Wallis and Dunn's tests compared to (i) untreated control; **** $p<0.0001$, (ii) Coating LR; #### $p<0.0001$, and (iii) Coating HR; §§§ $p<0.001$

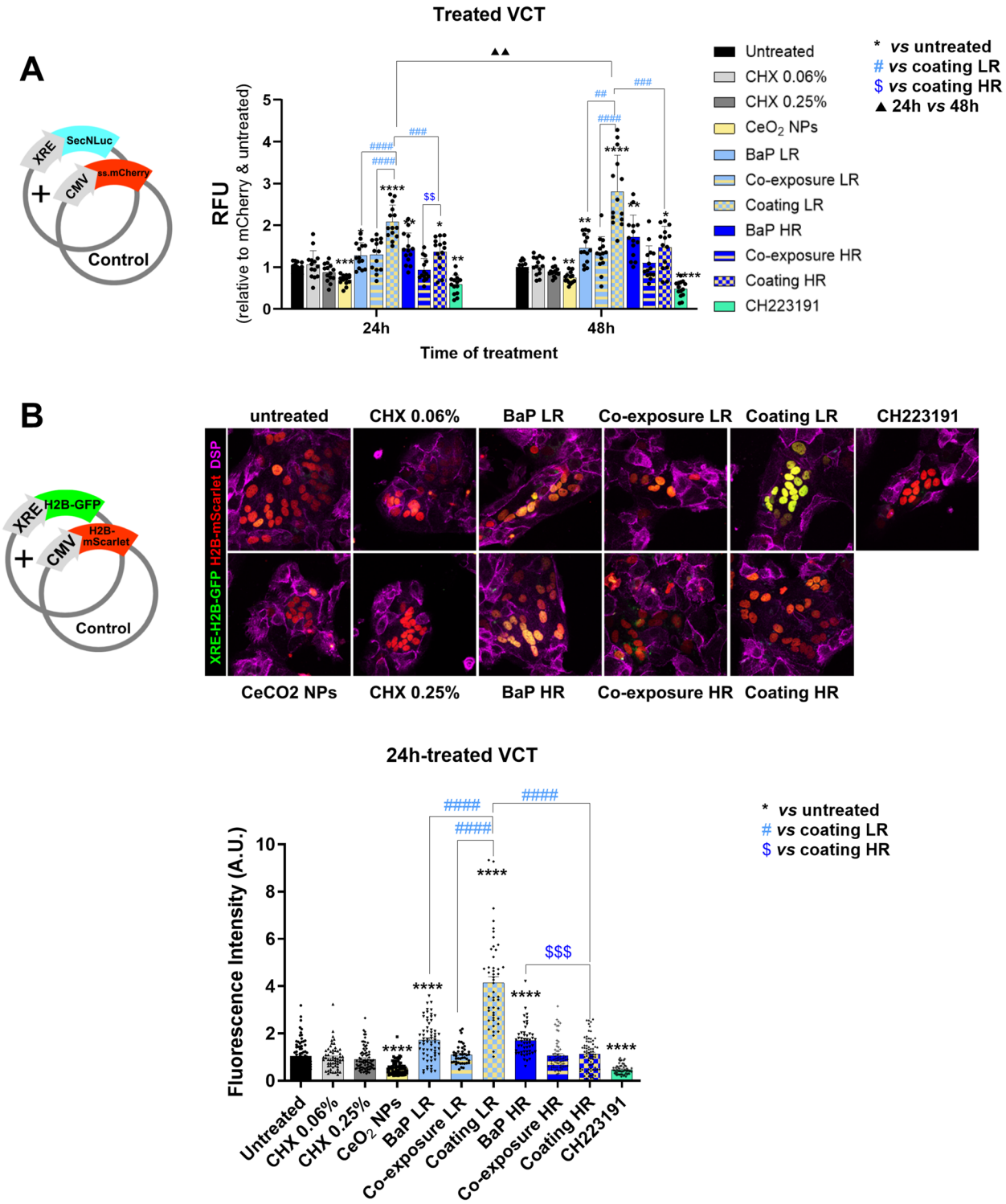

Fig. 1 (See legend on previous page.)

both 24 and 48 h of treatment (0.69 ± 0.11, 0.58 ± 0.22 versus 1 ± 0.11 at 24 h, $p < 0.001$) (Fig. 1A). In contrast, the treatments with Coatings at LR and HR (2.08 ± 0.40, 1.37 ± 0.37 versus 1 ± 0.11, $p < 0.05$ and $p < 0.001$), as well as BaP alone at concentrations of LR and HR (1.28 ± 0.30, 1.44 ± 0.37 versus 1 ± 0.11, $p < 0.05$ and

$p < 0.01$) significantly increased reporter gene activity after 24 h. Co-exposure at LR and HR, and vehicle treatments (CHX 0.06 and 0.25%) did not significantly modify reporter gene activity. Moreover, the results also showed a significant difference between the two ratios of coated NPs, interestingly, with higher effect for the lowest dose of BaP (e.g. Coating LR versus Coating HR, 2.08 ± 0.40 versus 1.36 ± 0.36, $p < 0.001$) (Fig. 1A). In addition, AhR activity was different between coating and co-exposure irrespective of the NPs/BaP ratio (e.g. Coating LR versus Co-exposure LR, 2.08 ± 0.40 versus 1.30 ± 0.37, $p < 0.0001$; and Coating HR versus Co-exposure HR, 1.36 ± 0.36 versus 0. 93 ± 0.27, $p < 0.01$), as well as between Coating at LR and BaP HR (2.08 ± 0.40 versus 1.28 ± 0.30, $p < 0.0001$) (Fig. 1A). These effects were slightly increased after 48 h of treatment for Coating LR (2.08 ± 0.40 at 24 h versus 2.81 ± 0.86 at 48 h, $p < 0.01$). In order to check that the presence of NPs does not affect the results, an NPs interference test on luminescence readings was carried out. The luminescence measurements obtained before and after centrifugation of supernatants containing NPs (to discard the NPs) or after addition of freshly prepared NPs in untreated supernatants, were close to 1, suggesting that NPs did not interfere with luminescence measurements (Figure S1).

Cytotrophoblast transfection with the XRE-H2B-eGFP plasmid induces GFP positive nuclei that reflect the intensity of plasmid reporter gene's transcriptional activation and thus AhR activity. In parallel, co-transfection with a CMV-H2B-mScarlet plasmid allowed monitoring of transfection efficiency. Confocal image quantification of the nuclear fluorescence signal intensity in VCT transfected with the XRE-H2B-eGFP plasmid (which induces GFP + nuclei reflecting AhR activity) confirmed the significant inhibition of AhR activity as early as 24 h of treatment with CeO_2 NPs alone (0.54 ± 0.28 versus 1 ± 0.57; $p < 0.001$), similar to AhR antagonist CH2223191 (0.47 ± 0.20, $p < 0.0001$), and the significant increase in AhR activity as early as 24 h of treatment with Coating LR (4.1 ± 1.8 versus 1 ± 0.57, $p < 0.0001$) (Fig. 1B and lower bar graph). Increased reporter activity was also obtained with BaP alone at both LR and HR concentrations (1.7 ± 0.82 or 1.7 ± 0.65 versus 1 ± 0.57, $p < 0.0001$) although to a lesser extent than with Coating at LR (4.1 ± 1.8). The other treatments had no significant difference in nuclei fluorescence reflecting the plasmid reporter gene activity (Fig. 1B and bar graph). Again, the results also show a significant difference between the two ratios of coated NPs (e.g. Coating LR versus Coating HR, 4.1 ± 1.8 versus 1.1 ± 0.67, $p < 0.0001$); between Coating and Co-exposure at LR (e.g. Coating LR versus Co-exposure LR, 4.1 ± 1.8 versus 1.1 ± 0.41, $p < 0.0001$); and between Coating and BaP at LR and HR (e.g. Coating LR versus BaP LR; 4.1 ± 1.8 versus 1.7 ± 0.82 $p < 0.0001$, Coating HR versus BaP HR 1.1 ± 0.67 versus 1.7 ± 0.65, $p < 0.05$). Interestingly, when BaP is coated on CeO_2 NPs, the trend is reversed between the two BaP ratios, with the lower dose inducing higher AhR activity, as evidenced by the activation of the XRE reporter gene (using XRE-Luc and XRE-GFP plasmids) (Fig. 1).

Impact of pollutants on cytotrophoblast differentiation/fusion capacity

Given the effects of the different NPs and BaP treatments on AhR activity, the second objective of this study was to assess the capacity of VCT to differentiate (by measuring the trophoblast fusion index) after exposure to these pollutants in coated form, co-exposed or individually exposed form. For this purpose, an immunofluorescence approach targeting the specific marker of mononucleated trophoblastic cells (GATA3) was selected, as previously validated and published [34]. Figure 2 showed that treatment with NPs alone significantly inhibited cytotrophoblast fusion compared with untreated cells (32 ± 4% versus 50 ± 4%; $p < 0.$ 0001), as did treatment with the AhR antagonist CH223191 (39 ± 2%, $p < 0.001$) (Fig. 2 and lower quantification plot). Treatments with Coating at HR, Co-exposures at LR and HR, and"vehicle"treatments (CHX 0.06 and 0.25%) did not significantly modify the syncytialization of cytotrophoblasts. The treatment with NPs coated with the lowest concentration of BaP (Coating LR), as well as those with BaP alone (both at LR and HR concentrations) significantly increased cytotrophoblast fusion capacity (72 ± 3%, 74 ± 5% and 69 ± 5% respectively versus 50 ± 4%, $p < 0.0001$) (Fig. 2 and lower graph quantification). Interestingly, the results also showed a significant difference between the two ratios of coated NPs (e.g. Coating LR versus Coating HR, 72 ± 3% versus 47 ± 4%, $p < 0.$ 0001); between Coating and Co-exposure at LR (e.g. Coating LR versus Co-exposure LR, 72 ± 3% versus 47 ± 4%, $p < 0.0001$), and also between Coating at HR and BaP at the concentration of HR (47 ± 4% versus 69 ± 5% <, $p < 0.0001$).

The significantly higher differentiation capacity of cytotrophoblasts observed upon exposure to the lowest coating ratio of BaP (Coating LR-NPs) was further investigated to determine whether this effect was mediated through the activation of the AhR-dependent pathway. To this end, cells were pretreated with an AhR antagonist (3 µM of CH223191) for 1 h before the addition of Coating LR. As previously, cytotrophoblasts differentiation capacity was assessed at 24 h post-treatment by immunostaining for the GATA3 marker (Fig. 3). The results showed induction and inhibition of cell differentiation

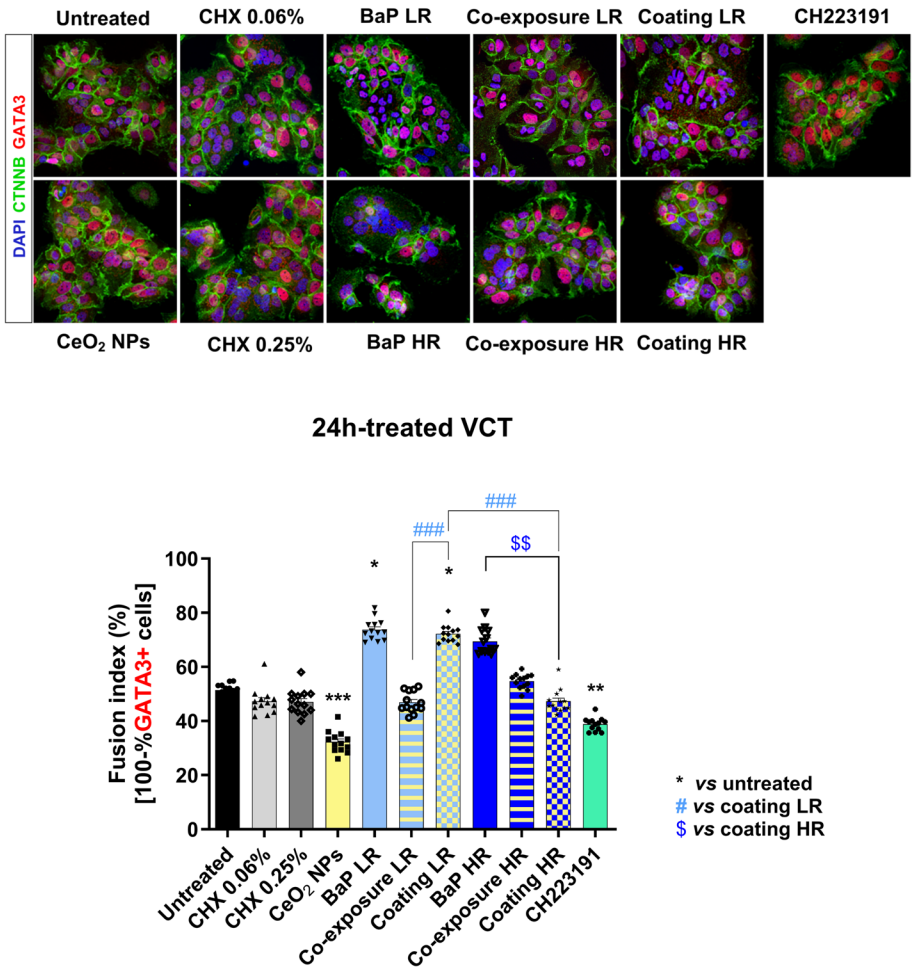

Fig. 2 Effect of BaP-coated CeO_2 NPs on trophoblast cell fusion. After 16 h of culture, VCT were treated for 24 h with 10 µg/cm^2 CeO_2 NPs (CeO_2 NPs), 10 µg/cm^2 CeO_2 NPs coated with 2 concentrations of BaP (Coating LR at 0.25 µM and Coating HR at 1 µM), 10 µg/cm^2 CeO_2 NPs co-exposed with 2 concentrations of BaP (Co-exposure LR at 0.25 µM and Co-exposure HR at 1 µM), 2 concentrations of BaP alone (BaP LR at 0.25 µM and BaP HR at 1 µM), 2"vehicle"controls due to BaP dilution in cyclohexane (CHX 0.06 and 0.25%) or 3 µM of AhR antagonist (CH223191). Representative images of cells fixed at 24 h and subjected to fusion assay (nuclei of mononuclear VCT were immunolabeled with anti-GATA3 antibody (red), membranes with anti-β-catenin (CTNNB, green) and nuclei were counterstained with DAPI (blue). Scale bar: 20 µm. (lower bar graph) Quantification of the fusion index. Nuclei were counted manually using the"cell counter"plugin of ImageJ. The fusion index (%) was calculated using the formula [100—% (number of GATA3$^+$ nuclei/total number of nuclei)]. Values are represented as mean ± SEM of the percentage ($n = 5$ placentas, 3 non-overlapping images per replicate). Statistical analysis was performed using Kruskal–Wallis and Dunn's tests against (i) untreated control; * $p < 0.05$, ** $p < 0.01$, *** $p < 0.001$, (ii) Coating HR; ### $p < 0.001$, and (iii) Coating HR; §§ $p < 0.01$

when cells were treated respectively with Coating at LR and AhR antagonist, as compared to the control (78 ± 6% and 35 ± 5% versus 46 ± 2%, $p < 0.0001$), confirming previous results (Fig. 2). Interestingly, there was a significant decrease in fusion capacity between trophoblasts treated with Coating at LR and those pre-treated with AhR inhibitor (78 ± 6% versus. 49 ± 4%, $p < 0.0001$), suggesting involvement of AhR (Fig. 3).

Effects of pollutants on mitochondrial network phenotype

Cytotrophoblast differentiation into syncytiotrophoblast is accompanied by major changes not only in cell morphology (trophoblast fusion) but also in mitochondrial structure and function. These mitochondrial modifications play a crucial role enabling the syncytiotrophoblast to acquire steroidogenic capacity [6, 8]. Thus, we evaluated the impact of these pollutants on this critical organelle following VCT exposure. An immunofluorescence approach was chosen to visualize the mitochondrial network, using an anti-COX2 antibody, a translocase involved in electron transport of the respiratory chain located at the inner mitochondrial membrane using high-resolution confocal STED microscopy. First of all, we checked whether we can reproduce the

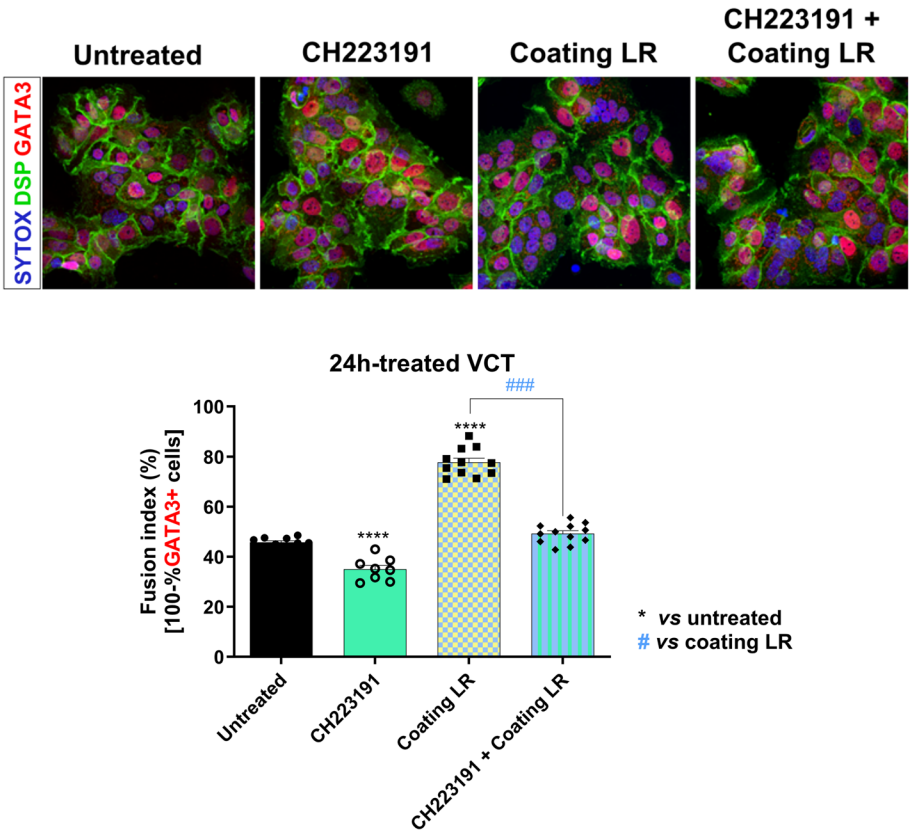

Fig. 3 Effect of pretreatment with an AhR inhibitor on the induction of cell fusion by Coating LR. After 16 h of culture, VCT were pretreated or not with 3 µM AhR antagonist (CH223191) for 1 h and then treated for 24 h with CeO_2 NPs coated with 0.25 µM BaP (Coating LR). Representative images of fixed cells after 24 h of treatment and subjected to fusion assay (nuclei of mononucleated VCT were immunolabeled with anti-GATA3 antibody (red), membranes with anti-desmoplakin antibody (DSP, green), and nuclei were counterstained with SYTOX Deep Red (blue)). Scale bar: 20 µm. (lower bar graph) Quantification of the fusion index. Nuclei were counted manually using the"cell counter"plugin of ImageJ. The fusion index (%) was calculated according to the formula [100—% (number of $GATA3^+$ nuclei/total number of nuclei)]. Values are represented as mean ± SEM of the percentage ($n = 4$ placentas, 3 non-overlapping images per replicate). Statistical analysis was performed using a one-way ANOVA Dunnett test against (i) untreated control; **** $p < 0.0001$, and (ii) coating HR; #### $p < 0.0001$

mitochondria network modifications between VCT and ST, previously observed by TEM in tissues [8, 9, 42] in conditions when VCT are purified from term placenta and cultured as primary trophoblasts that further differentiate to form the ST. Figure S2 showed that VCT at 24 h of culture harbor a classical mitochondrial network, highly interconnected and with a tubular mitochondrial shape. During the syncytialization, achieved spontaneously after 24 h to 72 h of culture, the mitochondrial network undertakes extensive fragmentation leading to small mitochondria with spherical morphology and poor interconnections (Figure S2).

After VCT exposure to pollutants, the results showed a dichotomy in mitochondrial network morphology and interconnectivity between cells treated with CeO_2 NPs and those with BaP (Fig. 4A, red frames versus green frames). In trophoblasts exposed to CeO_2 NPs for 24 h, whatever the conditions: alone, coated or co-exposed (CeO_2 NPs, Coating LR and HR, Co-exposure LR and HR), mitochondria appear longer with a tubular shape and the network is denser and more interconnected (Fig. 4B, red violins plots); whereas BaP treatments (LR and HR) are similar to the control (CHX 0.25%), showing a classic mitochondrial network (Fig. 4B, green violins plots).

Next, a deeper comparative study was undertaken with cells treated with CeO_2 NPs alone for 24 h (Fig. 5). VCT treated with CeO_2 NPs present a significantly higher number of mitochondria compared with controls (372 ± 142 versus 237 ± 96, $p < 0.001$) and a significantly higher total volume (372 μm^3 ± 142 versus 236 μm^3 ± 96, $p < 0.01$) (Fig. 5B quantifications plots). In addition, mitochondria are longer and thinner in CeO_2 NPs-treated conditions resulting in a significantly lower sphericity (0.142 ± 0.04 versus 0.189 ± 0.06, $p < 0.01$) and a significantly higher branch length (6.44 µm ± 2.12

versus 4.20 µm ± 1.45, $p < 0.001$) and a denser mitochondrial network connectivity with a significantly higher number of branches and number of junctions compared to controls (9.20 ± 3.48 versus 5.24 ± 1.63, and 4.41 ± 1 0.61 versus 2.41 ± 1.11, $p < 0.0001$) (Fig. 5B quantifications plots). These results suggest that exposure of VCT to CeO_2 NPs induces an elongation of the mitochondrial network, whereas BaP has no major impact on the mitochondrial phenotype.

Effects of CeO_2 NPs on mitochondrial dynamics regulators

In view of the observed changes in trophoblast mitochondrial network morphology induced by CeO_2 NPs exposure, we further investigated the mechanisms underlying these modifications. In order to determine whether the effects were specifically due to CeO_2 NPs or simply to the presence of NPs, we tested the addition of other metallic dioxide nanoparticles, ZrO_2 NPs, which are considered biocompatible [43] and non-cytotoxic to human trophoblastic cell lines [44]. To investigate the impact of CeO_2 NPs on mitochondrial dynamics in exposed VCT, we analyzed variations in both transcript and protein levels of key mitochondrial fusion (MFN 1 and 2, and OPA1) and fission (DRP1 and FIS1) machineries (Fig. 6). No significant changes were observed in the transcripts or protein levels of fusion players after treating VCT with CeO_2 NPs compared to the untreated control (Fig. 6A). The only observed modifications were induced by CHX, the solvent used for coating, on *OPA1* transcript levels (1.95 ± 0.26 versus 1.32 ± 0.29, $p < 0.05$) and with ZrO_2 NPs (1.95 ± 0.13 versus 1.32, $p < 0.05$) treatment (Fig. 6A). The variations in *OPA1* transcript levels were not visible at the protein level. Exposure to CeO_2 NPs did not alter the transcription or protein levels of DRP1 and FIS1, compared to the untreated control (Fig. 6B).

To complete the study on mitochondrial changes, we evaluated the potential impact of CeO_2 NPs on mitochondrial biogenesis – a process by which cells increase mitochondrial numbers – by analyzing variations in the transcript levels of peroxisome proliferator-activated receptor gamma coactivator 1-alpha (*PGC-1α*) and in the protein levels of VDAC1 (Fig. 6C).We chose to analyze the transcript levels of *PGC-1α*, a key transcriptional coactivator that regulates the expression of various mitochondrial respiratory chain complex subunits and mtDNA replication, all of which are essential for mitochondrial biogenesis. Additionally, determining the protein level of VDAC1, a highly abundant β-barrel protein of the mitochondrial outer membrane, can provide insights into the overall cellular mitochondrial content. However, there were no significant changes in either *PGC-1α* transcript levels or VDAC1 protein levels when VCT were exposed to CeO_2 NPs, nor with the other treatments (Fig. 6C). Therefore, we did not find any changes in the players of mitochondrial dynamics or biogenesis that could explain the alterations in the mitochondrial network phenotype following VCT exposure to CHX-treated CeO_2 NPs.

Effects of pollutants on mitochondrial transmembrane potential

The morphological changes observed in the mitochondria network during VCT differentiation are associated with a functional and metabolic shift, transitioning from ATP energy production to steroid hormone synthesis (steroidogenesis) [9]. Thus, we next evaluated mitochondrial functionality following exposure to pollutants by measuring the mitochondrial inner membrane potential (ΔΨm) using the JC-1 probe (Fig. 7). JC-1 is a cationic dye that accumulates in mitochondria in a membrane potential-dependent manner, causing a fluorescence emission shift from green (monomeric form, ~ 525 nm) to red (aggregated form, ~ 590 nm). Figure 7 shows that a 48 h treatment with CeO_2 NPs alone significantly increased ΔΨm as compared to the untreated control (1.41 ± 0.37 versus 1 ± 0.05; $p < 0.001$) (Fig. 7A and lower quantification plot). Treatments with CeO_2 NPs coated with the lowest concentration of BaP (Coating LR), as well as those with BaP alone (LR and HR) had opposite effects and significantly inhibited ΔΨm (0.49 ± 0.16,

(See figure on next page.)

Fig. 4 Effects of CeO_2 NPs on the morphology and network of mitochondria. After 16 h of culture, VCT were treated for 24 h with 10 µg/cm^2 CeO_2 NPs (CeO_2 NPs), 10 µg/cm^2 CeO_2 NPs coated with 2 concentrations of BaP (Coating LR at 0.25 µM and Coating HR at 1 µM), 10 µg/cm^2 CeO_2 NPs co-exposed with 2 concentrations of BaP (Co-exposure LR at 0.25 µM and Co-exposure HR at 1 µM), 2 concentrations of BaP alone (BaP LR at 0.25 µM and BaP HR at 1 µM) and the highest concentration of the vehicle control cyclohexane solvent (CHX 0.25%). After fixation, cells were immunolabeled with anti-COX2 (mitochondrial inner membrane marker) antibody and observed under a super-resolution STED microscope. **A** Representative images of VCT mitochondrial networks. In the green box, representative images of VCT treated with CHX solvent and the 2 BaP concentrations, and in red box representative images of VCT treated with NPs (NPs alone, NPs coated and co-exposed with BaP). Scale bar: 10 µm. **B** Quantitative analysis of mitochondrial network parameters using the "Mitochondria Analyzer" plugin of ImageJ. Comparison of six mitochondrial parameters (mitochondrial count, total volume, sphericity, branches, branch junctions, and branch length) between control conditions (CHX, BaP LR, BaP HR) and NP-treated conditions (CeO_2 NPs, Coating LR, Coating HR, Co-exposure LR, Co-exposure HR). Values are represented as "violin" plots. Statistical analysis was performed using Student's *t* test comparing NP-treated conditions against controls; *$p < 0.05$, **$p < 0.01$

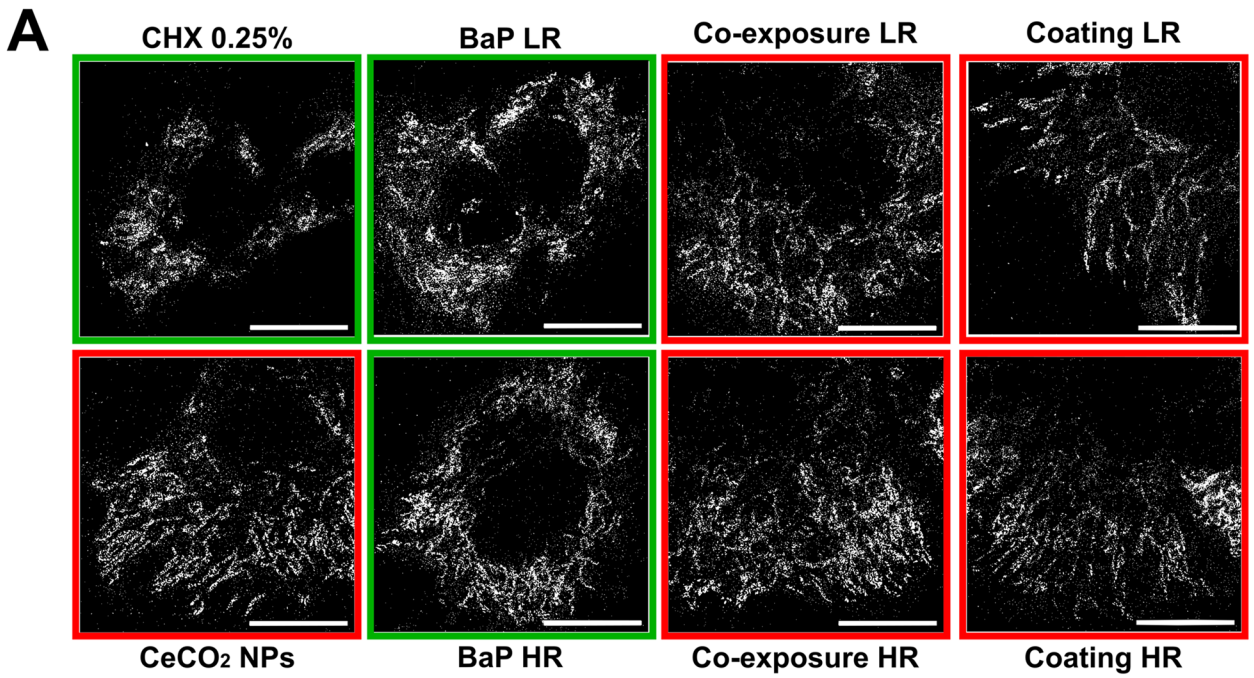

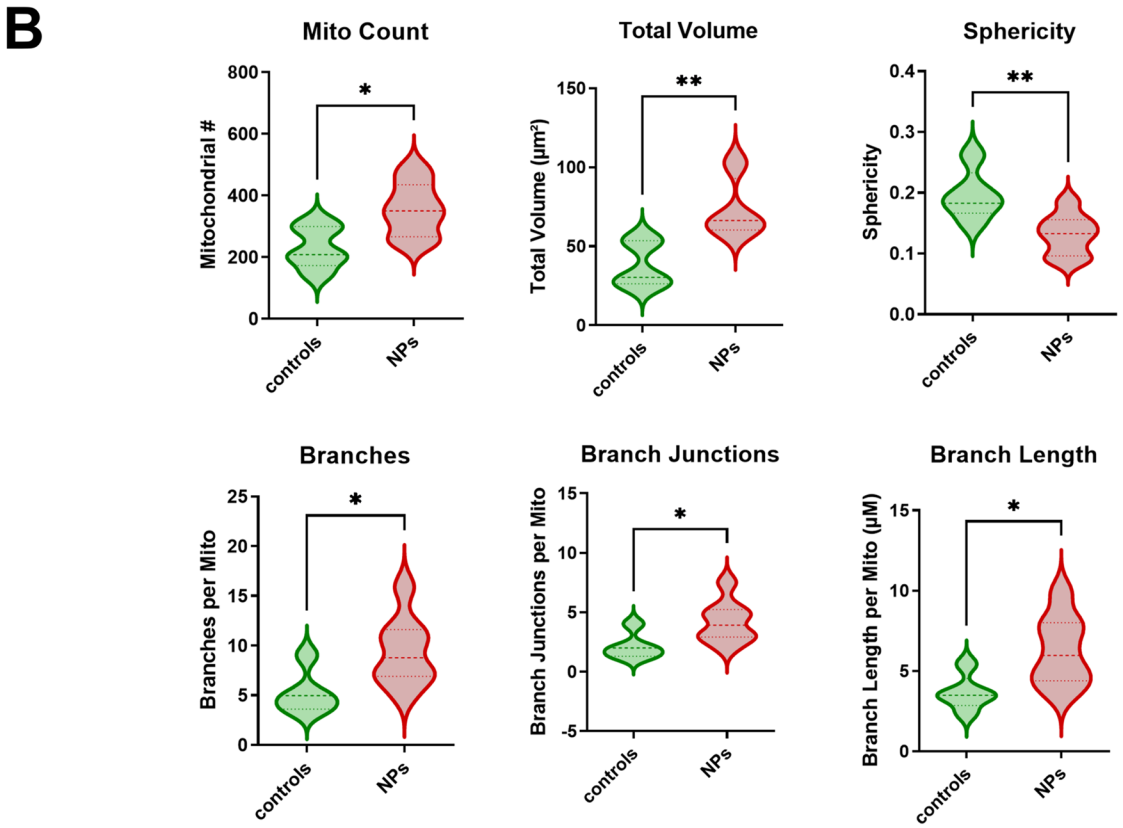

Fig. 4 (See legend on previous page.)

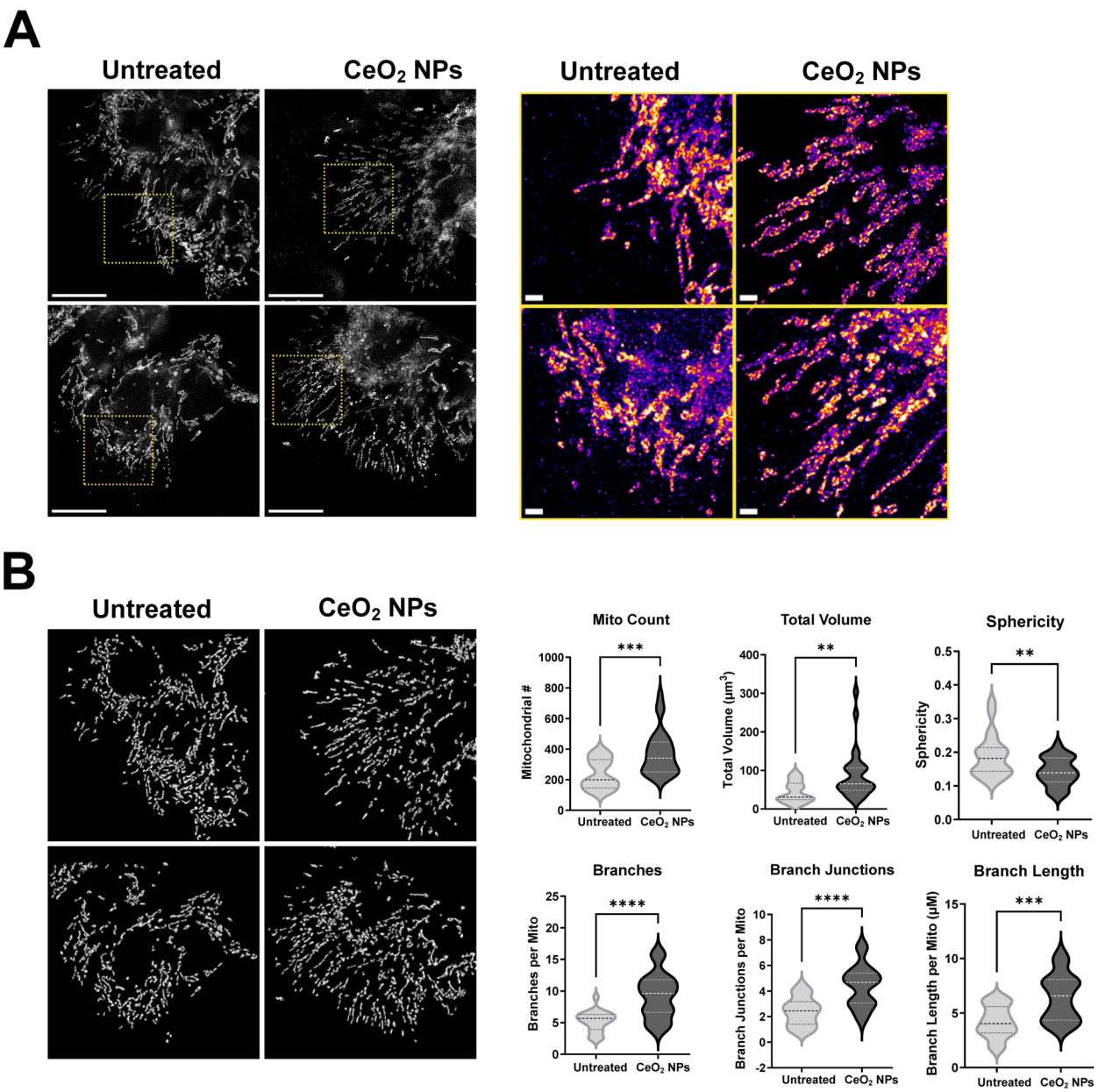

Fig. 5 Increase in VCT mitochondrial network connectivity after treatment with CeO_2 NPs. After 16 h of culture, VCT were treated or not with 10 µg/cm^2 CeO_2 NPs [NPs] for 24 h. After fixation, cells were immunolabeled with anti-COX2 (mitochondrial inner membrane marker) antibody and observed under a STED super-resolution microscope. **A** left panel, 2 representative images of STED images after deconvolution for each condition and right panel, image magnification of the left panel with the use of ImageJ "fire" LUT. Scale bar: 10 µm. **B** Analysis of the morphology and network of mitochondria by the"Mitochondria Analyzer"plugin of ImageJ. Left panel, 2 representative images of the post-analyzed STED images from A for each condition. Right panel, quantification and comparison of the different mitochondrial parameters between the control and NPs-treated cells. Values are represented as"violin"($n = 6$ experiments, 3–5 non-overlapping images per replicate). Statistical analysis was performed using Student's t test against untreated control cells; ** $p < 0.01$, *** $p < 0.001$, **** $p < 0.0001$

0.74 ± 0.08 and 0.59 ± 0.18, respectively versus $1 \pm 0.$ 05; $p < 0.0001$, $p < 0.01$, $p < 0.001$), similar to that of treatment with 1 µM Stau, an apoptotic inducer used as a positive control for mitochondrial membrane potential depolarization ($\Delta\Psi$m drop, 0.62 ± 0.09, $p < 0.0001$). All the other treatments, such as with Co-exposure at LR and HR, Coating at HR,"vehicle"(CHX at 0.06 and 0.25%) and AhR antagonist (CH223191, 3 µM) did not significantly alter $\Delta\Psi$m. Moreover, the results also showed a significant difference between the two doses of BaP-coated CeO_2 NPs

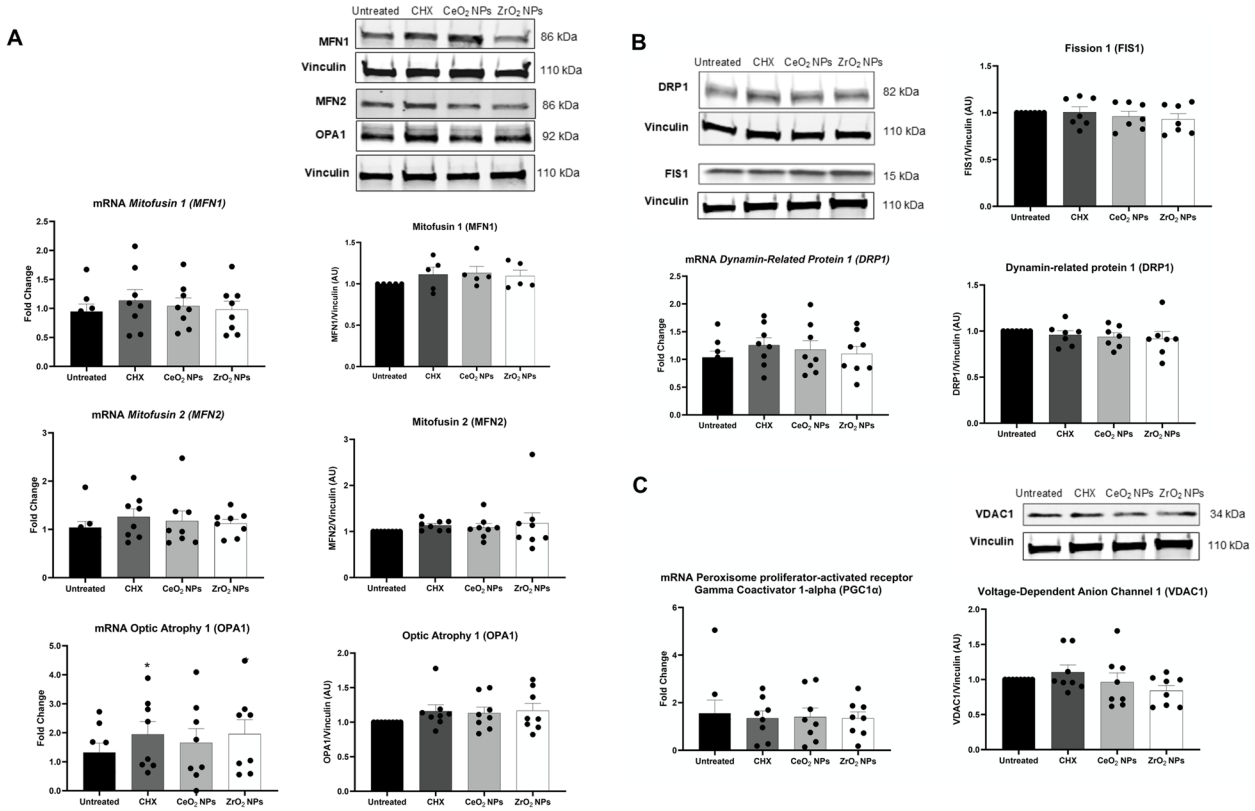

Fig. 6 Effects of CeO_2 NPs on mitochondrial dynamics regulators. VCT purified from term placentas were plated overnight and left untreated or incubated for 48 h with 10 µg/cm^2 CeO_2 NPs (CeO_2), 10 µg/cm^2 ZrO_2 NPs (ZrO_2), and the vehicle control cyclohexane solvent (CHX 0.25%). Total mRNA was extracted from VCT, followed by reverse transcription. The 3 reference genes used were *RPL13*, *RPLP0*, and *SDHA*. The relative amounts of mRNA were estimated using the Pfaffl method. The results, expressed as fold change, represent the mean + SEM ($n = 8$). Total protein extracts were subjected to SDS-PAGE under reducing conditions. Immunoblots were quantified with an Odyssey System Imager and the results represent the mean + SEM after normalization to vinculin ($n = 8$ and $n = 5$ for MFN1). Statistical analysis was performed using the one-way ANOVA Dunnett test; * $p < 0.05$ versus untreated. **A** RT-qPCR was performed for the genes of interest *MFN1*, *MFN2* and *OPA1*. Membranes were immunoblotted with anti-MFN1, anti-MFN2, anti-OPA1, and anti-vinculin antibodies (loading control). **B** RT-qPCR was performed for the gene of interest *DRP1*. Membranes were immunoblotted with anti-DRP1, anti-FIS1 and anti-vinculin antibodies (loading control). **C** RT-qPCR was performed for the gene of interest *PGC-1α*. Membranes were immunoblotted with anti-VDAC1, and anti-vinculin antibodies (loading control)

(e.g. Coating LR versus Coating HR, 0.49 ± 0.16 versus 1 ± 0.18, $p < 0.0001$), between Coating and Co-exposure at LR (e.g. Coating LR versus Co-exposure LR, 0.49 ± 0.16 versus 0.94 ± 0.14, $p < 0.0001$), and between Coating and BaP (e.g. Coating LR versus BaP LR, 0.49 ± 0.16 versus 0.74 ± 0.0.08 $p < 0.05$; and Coating HR and BaP HR, 1 ± 0.18 versus 0.59 ± 0.18, $p < 0.01$). It is noteworthy that the difference in ΔΨm was reversed between the two studied doses of BaP. These differences in ΔΨm appeared only at 48 h of treatment, when the majority of VCT are differentiated into ST, whereas no significant changes were observed at 24 h except for BaP HR (Figure S3). Overall, the ratios observed in Fig. 7 were inversely proportional to those of the fusion index (Fig. 2). Moreover, after immunostaining of JC-1-stained cells with the anti-cadherin antibody (a membrane marker) and counterstaining nuclei with DAPI, the two cell types (VCT or ST) could be distinguished after 48 h of treatment. The staining highlighted a loss of mitochondrial transmembrane potential, predominantly in ST (Figure S4). In fact, the monomeric-green form was mostly observed in ST, whereas both forms (monomeric-green and aggregated-red) were present in VCT suggesting that the change in transmembrane potential was due to the impact of pollutants on trophoblast differentiation capacity rather than to a direct drop in ΔΨm within VCT.

Effects of pollutants on mitochondrial respiration

Given the observed effects of BaP and CeO_2 NPs on mitochondrial membrane potential, we subsequently investigated their impact on mitochondrial respiration using the XFe24 Seahorse Analyzer to measure the OCR (Figs. 8 and S5). Basal respiration was significantly reduced only by Co-exposure at LR, with a 15.7% ± 2.9

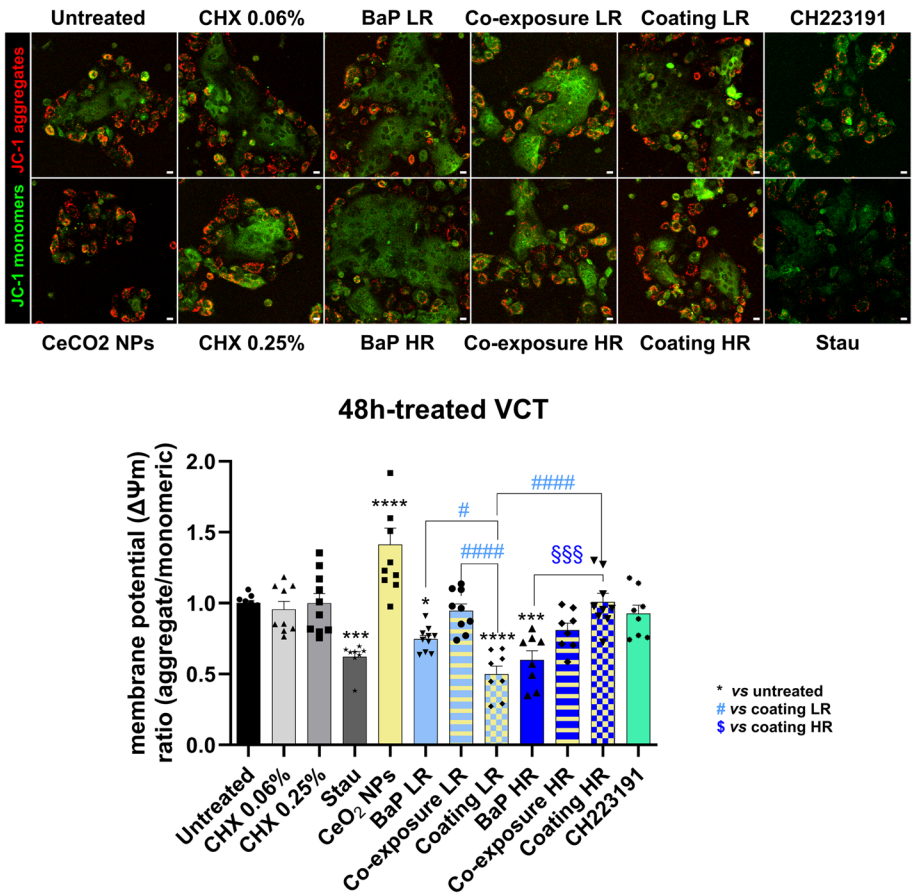

Fig. 7 Effects of BaP-coated CeO_2 NPs on the mitochondrial membrane potential of VCT treated for 48 h. After 16 h of culture, VCT were treated for 48 h with 10 µg/cm^2 CeO_2 NPs (CeO_2 NPs), 10 µg/cm^2 CeO_2 NPs coated with 2 concentrations of BaP (Coating LR at 0.25 µM and Coating HR at 1 µM), 10 µg/cm^2 CeO_2 NPs co-exposed with 2 concentrations of BaP (Co-exposure LR at 0.25 µM and Co-exposure HR at 1 µM), 2 concentrations of BaP alone (BaP LR at 0.25 µM and BaP HR at 1 µM), 2"vehicle"controls due to BaP dilution in cyclohexane (CHX 0.06 and 0.25%), 3 µM of AhR antagonist (CH223191) or 1 µM staurosporine (Stau) as positive depolarization control. After treatments, cells were incubated for 30 min at 37 °C with 1 µM of JC-1 dye. Representative images of fixed cells are shown at the top of the figure. In green, the monomeric form and in red, the aggregated form of JC-1 dye. Scale bar: 10 µm. (lower bar graph) Quantification of membrane potential (ΔΨm) corresponding to the ratio of fluorescence intensities of the aggregated form (Ex/Em: 570/590) to the monomeric form (Ex/Em: 514/530). Values are presented as the mean + SD of the normalized ratios to untreated cells ($n = 4$ with technical triplicate). Statistical analysis was performed using a one-way ANOVA against (i) untreated control; * $p < 0.05$, *** $p < 0.001$, **** $p < 0.0001$, (ii) Coating LR; # $p < 0.05$, #### $p < 0.0001$, and (iii) Coating HR; $$$ $p < 0.001$

(See figure on next page.)

Fig. 8 Effects of BaP-coated CeO_2 NPs on mitochondrial respiration of VCT treated for 24 h. After 16 h of culture, VCT were treated for 48 h with 10 µg/cm^2 CeO_2 NPs (CeO_2 NPs), 10 µg/cm^2 CeO_2 NPs coated with 2 concentrations of BaP (Coating LR at 0.25 µM and Coating HR at 1 µM), 10 µg/cm^2 CeO_2 NPs co-exposed with 2 concentrations of BaP (Co-exposure LR at 0.25 µM and Co-exposure HR at 1 µM), 2 concentrations of BaP alone (BaP LR at 0.25 µM and BaP HR at 1 µM), solvent controls due to BaP dilution in cyclohexane (CHX 0.25%), pre-treated or not with 3 µM AhR antagonist (CH223191) for 1 h and then treated for 24 h with CeO_2 NPs coated with 0.25 µM BaP (CH223191 + Coating LR). To measure different oxygen consumption rate (OCR) parameters, selective inhibitors were injected: oligomycin (1.5 µM), carbonyl cyanide-4 phenylhydrazone (FCCP, 1 µM), rotenone (0.5 µM) and antimycin A (0.5 µM). OCR values were normalized to the amount of DNA content from each well using Hoechst' stain. Values are presented as the mean ± SEM of the percentage of OCR relative to untreated cells ($n = 5$ with technical quadruplicate). Statistical analysis was performed using one-way ANOVA against (i) untreated control; * $p < 0.05$, ** $p < 0.005$

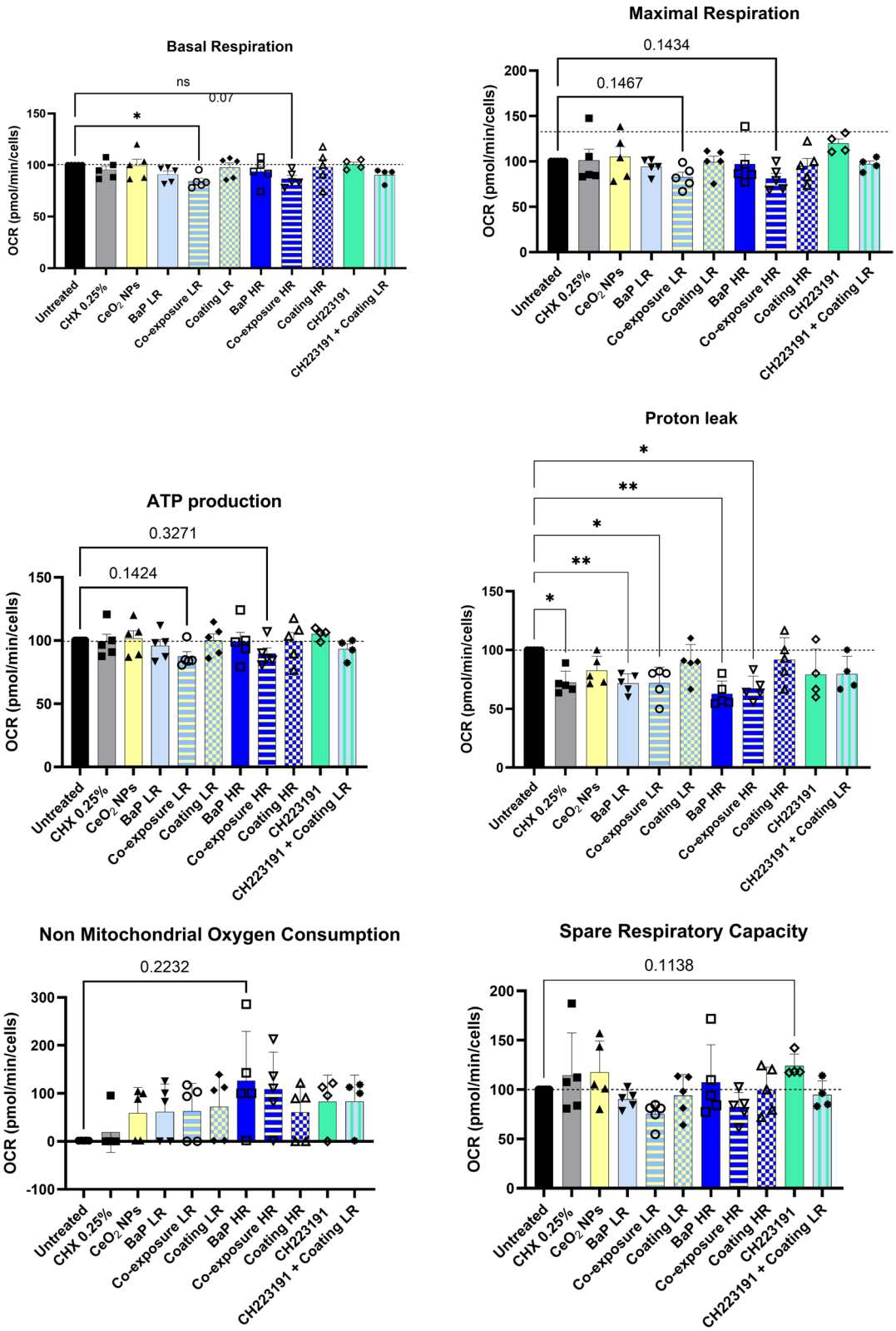

Fig. 8 (See legend on previous page.)

SEM decrease in OCR compared to the control ($p < 0.05$). A similar trend was observed with co-exposure at HR (decrease of 13.2% ± 3.3 SEM, $p = 0.07$), although this decrease was not statistically significant. Regarding maximal mitochondrial respiration and ATP production, none of the experimental conditions significantly decreased OCR, although decreasing trends were observed for both LR and HR co-exposures ($p = 0.14$). Regarding proton leak, the CHX solvent significantly reduced it, with a decrease of 27.8% ± 4.4 SEM in OCR compared to the control ($p < 0.05$), as did most treatments. However, no significant effect was observed for CeO_2 NPs, the coatings at LR and HR, nor for the AhR inhibitor CH223191. Finally, none of the treatments significantly altered non-mitochondrial oxygen consumption or spare respiratory capacity compared to the control.

Effects of CeO_2 NPs on the production of sex steroids and oxysterols

To further investigate the functional status of the mitochondrial network, sex steroid hormones and oxysterols produced by trophoblasts exposed to 10 µg/cm^2 CeO_2 NPs for 48 h were quantified in culture supernatants (Fig. 9). An increase in E1 levels was detected after 48 h exposure to CeO_2 NPs (59.3 ± 3.8 SEM ng/g protein compared to the control at 56.2 ± 4.1 SEM, $p < 0.05$, Fig. 9A). Conversely, a decrease in DHEA levels was observed (2.5 ± 0.2 SEM ng/g protein compared to the control at 3.3 ± 0.2 SEM, $p < 0.05$, Fig. 9A). Since placental sex can influence hormone production [45], steroid quantifications were also analyzed separately for male and female placentas. The increase in E1 after exposure to CeO_2 NPs was significant only in trophoblasts from female placentas (58.6 ± 3.7 SEM ng/g protein in treated VCT compared to untreated VCT at 54.3 ± 3.9 SEM, $p < 0.05$, Figure S6A), whereas the decrease in DHEA was observed exclusively in male placentas (2.4 ± 0.3 SEM ng/g protein in treated VCT compared to untreated VCT at 3.5 ± 0.2 SEM, $p < 0.05$, Figure S6A). Regarding the other quantified steroid hormones (T, E2, P4, 17OHP, DHT, A4) and oxysterols (7aOHC, 7bOHC, 5b6b Echol, 25OHC, 7KChoL, 4bOHC), no significant variations were detected between CeO_2 NPs-treated VCT and the untreated control. However, it is important to note that significant differences in the levels of certain sex steroids were observed between male and female placentas. VCT from male placentas treated with CeO_2 NPs exhibited higher levels of DHT compared to treated VCT from female placentas (1.2 ± 0.1 SEM ng/g protein compared to treated VCT from female placentas at 0.7 ± 0.1 SEM, $p < 0.05$, Figure S6A). In agreement, some oxysterols, such as 5b6b Echol (21.4 ± 4.5 SEM mg/g protein compared to treated VCT from female placentas at 9.9 ± 2.1 SEM, $p < 0.05$, Figure S6B) and 25OHC (2.9 ± 0.1 SEM versus 1.9 ± 0.1 SEM, $p < 0.05$ for control group and 2.9 ± 0.3 SEM versus 1.8 ± 0.1 SEM for treated VCT, $p < 0.05$, Figure S6B) exhibited higher levels in male placentas compared to their female counterparts regardless of treatments (untreated and treated VCT).

Uptake of BaP-coated NPs by the chorionic villi

In previous publications [21, 46], we demonstrated that both BaP and CeO_2 NPs can be internalized in placental tissues and trophoblasts following individual exposures in a dose- and time-dependent manner. CeO_2 NPs were observed forming aggregates in a peri-nuclear zone [23] whereas BaP exhibited a more diffuse intracellular distribution [46]. Here, we explored whether BaP-coated CeO_2 NPs could be absorbed by trophoblasts in primary culture, and whether differences exist between the two BaP doses when coated on CeO_2 NPs. Confocal microscopy was chosen to detect BaP of coated CeO_2 NPs, taking advantage of BaP's intrinsic fluorescence under UV excitation (Figure S7) [47]. In parallel, immunostaining for GATA3 (marker of undifferentiated VCT), E-catherin (membrane marker), and SYTOX (nuclear stain) was performed to distinguish VCT from ST. Aggregates were observed in cells treated for 48 h with BaP-coated CeO_2 NPs, with larger and more abundant aggregates detected in cells exposed to CeO_2 NPs coated with the highest BaP concentration (1 µM versus 0.25 µM) (Fig. 10A).

In our previous publication [21, 46], we demonstrated that both CeO_2 NPs and BaP are internalized in placental cells after exposure of trophoblasts. Here, we wanted to know whether BaP-coated CeO_2 NPs were also taken up by placental tissues. For this, placental villi cultured on agarose were pretreated with a lipid raft inhibitor by cholesterol depletion (10 mM MβCD) or a clathrin-mediated endocytosis inhibitor (450 mM sucrose) before exposure to BaP-coated CeO_2 NPs. Again, BaP was detected under UV by confocal microscopy. In parallel, we used staining with anti-CK7 antibody to identify the trophoblast layer from the rest of the tissue, SYTOX Deep Red for nuclear staining and anti-CD31 antibody to highlight endothelial mesenchymal vessels (Fig. 10B). To complete this study, a set of controls was carried out in order to validate the observations of Coating HR aggregates under UV in relation to the tissue background in different conditions, i.e. in the absence or presence of 10 mM MβCD, 450 mM sucrose, CHX 0.25%, 1 µM BaP (BaP HR) or 10 µg/cm^2 CeO_2 NPs alone (Fig. 10C). We observed internalization of BaP upon treatment of chorionic villi explants with BaP-coated CeO_2 NPs (HR) in the trophoblast layer as well as in the mesenchymal axis. This differs from BaP in individual exposure, where a more diffuse signal was observed, suggesting that the aggregates detected under

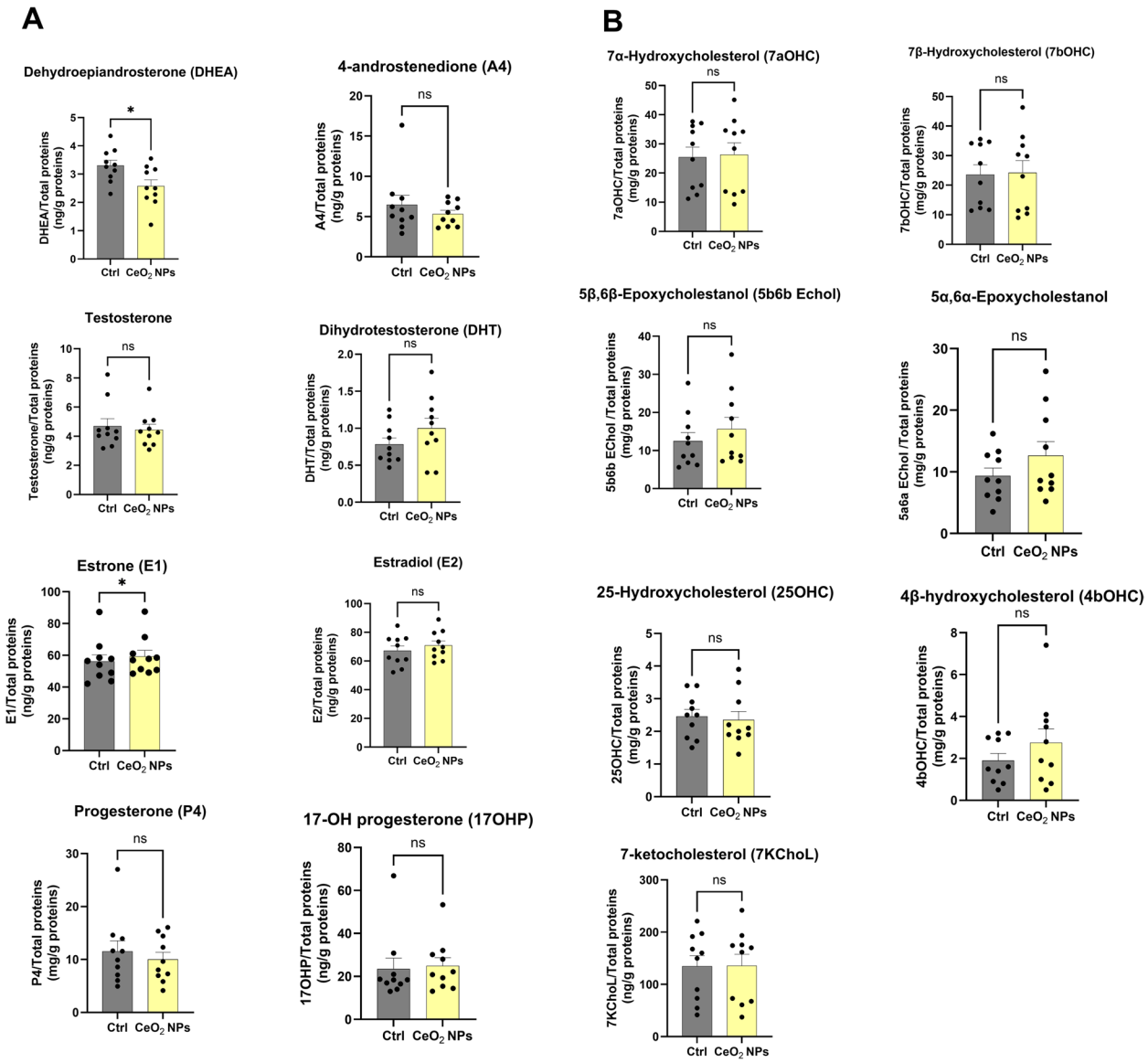

Fig. 9 Effects of CeO_2 NPs on steroids and oxysterol production by VCT treated for 48 h. VCT purified from term placentas were plated overnight and were left untreated or incubated for 48 h with 10 µg/cm^2 CeO_2. **A** The supernatants were collected, and the following steroid hormones were measured by GC–MS/MS: testosterone, estrone (E1), estradiol (E2), progesterone (P4), 17-OH progesterone (17OHP), dihydrotestosterone (DHT), dehydroepiandrosterone (DHEA), 4-androstenedione (A4). **B** The following oxysterols were measured by GC–MS/MS: 7α-hydroxycholesterol (7aOHC), 7β-hydroxycholesterol (7bOHC), 5β,6β-epoxycholestanol (5b6b Echol), 25-hydroxycholesterol (25OHC), 7-ketocholesterol (7KChoL), 4β-hydroxycholesterol (4bOHC). The hormone values were normalized to the protein content in supernatants. Values are presented as the mean ± SEM ($n = 10$). Statistical analysis was performed using t-test; * $p < 0.05$ versus Ctrl

confocal microscopy were likely due to BaP still present on CeO_2 NPs rather than free BaP distribution. As compared to coating at HR, pre-treatment with MβCD inhibited BaP-coated CeO_2 NPs internalization, whereas pre-treatment with sucrose had no effect (Fig. 10B). In conclusion, placental villi can internalize BaP-coated CeO_2 NPs, which appear as aggregates under UV light, with a higher uptake observed at the higher BaP dose (1 µM). This internalization process appears to be mediated by lipid rafts.

Discussion

In the present study, we investigated the impact of CeO_2 NPs on the human placental barrier when mixed with BaP, a prototype PAH, from common sources of emissions. To orient the reader, we first recall the composition

of the two BaP-coating ratios and the non-cytotoxic exposure concentrations derived from our previous work. To this end, we have previously produced and characterized [24] two ratios of BaP-coatings on CeO_2 NPs: one representative of the PAH/UFP ratio found in atmospheric pollution (Coating LR) (e.g. from 0.15 to 2 mg PAH per µg of UFP [25], of 1.66 mg BaP/g CeO_2 NPs) and a higher ratio of 6.63 mg BaP/g CeO_2 NPs (Coating HR), four times higher than the low ratio. The CeO_2 NPs used in this study had an average surface concentration of 10 µg/cm^2, a level that, according to our previous study [21], does not affect VCT viability (24–48 h) but disrupts trophoblast morphological and functional differentiation. Regarding BaP, primary trophoblast viability was only impacted above 2 µM after 72 h [23]. However, we previously showed that at non-cytotoxic levels (0.1–1 µM), BaP activated the AhR-dependent detoxification pathway, inducing CYP1A1, cell stress factors (p53, p21), and DNA damage markers (γ-H2AX) [23].

AhR activation and bioavailability of BaP

In this study, we investigated the effects of different types of exposure to CeO_2 NPs and BaP (co-exposure by simultaneous addition, exposure to BaP-coated CeO_2 NPs, and individual exposures) at concentrations that, according to our last study [24], do not significantly alter trophoblast viability. Using XRE-reporter gene plasmids (with xenobiotic response elements that ligand-activated AhR is able to recognize), we assessed the activity of AhR, synonymous with BaP metabolism and bioactivation, following exposure of human trophoblasts to these conditions. We showed here that both reporter gene plasmids were activated after exposure to BaP alone (0.25 or 1 µM) but also to BaP-coated CeO_2 NPs at the lowest BaP ratio, corresponding to 0.25 µM if all BaP desorbs from the NPs. Interestingly, activation was twice as high when trophoblasts were exposed to BaP-coated CeO_2 NPs (Coating LR) than to BaP alone. The fact that greater AhR-activation is observed with BaP-coated CeO_2 NPs than with BaP alone suggests that lipophilic BaP could facilitate internalization of CeO_2 NPs and that BaP could then be stabilized in cells by the coating on CeO_2 NPs, as a pool of available BaP, making it accessible to induce the detoxification pathway. Thus, the kinetics of plasmid activation, and BaP-metabolization, may be delayed by BaP coating on the CeO_2 NPs. Surprisingly, the coating LR activates the AhR pathway more intensively than the coating HR. We hypothesized that the ability of BaP to desorb from CeO_2 NPs and to be bioavailable for AhR activation would be reduced when coated at a high ratio due to the hydrophobicity of BaP. This is because BaP molecules in the corona of the CeO_2 NPs are more numerous when the ratio is higher, so they can more easily interact with each other. Conversely, trophoblast exposures to CeO_2 NPs alone decreased AhR-activation and this result was unexpected. Absence of AhR-activation by CeO_2 NPs is predictable because CeO_2 NPs cannot be detoxified by the conventional AhR-pathway in cells. However, the decrease in plasmid activation may suggest that CeO_2 NPs could interfere with nuclear factors or transcriptional machinery. In the literature, it is known that NPs have effects on transcription factors [48], notably by cytoplasmic sequestration of proteins, or by interference with the transcription machinery which could explain the reduction in AhR activity observed here. For instance, NPs can interfere with gene induction and post-transcriptional modifications of proteins once NPs are internalized in cells, as previously reported for other nuclear proteins [48]. Additionally, one could also hypothesize that NPs sequester endogenous AhR ligands, further contributing to this decrease in activity. To verify that CeO_2 NPs do not directly interfere with the luminescence readings, we included controls that excluded this hypothesis (Figure S1). It has been described that molecules including proteins can be adsorbed on the reactive surface of NPs. Proteins bound to NPs could simply be sequestrated, preventing them from functioning properly. The adsorption mechanism can occur in vitro as soon as the NPs come into contact with the culture medium, but also in trophoblasts in which they are internalized. In vivo, this adsorption can take place during contact of NPs with maternal blood. These molecules (including

(See figure on next page.)

Fig. 10 Internalization of BaP-coated CeO_2 NPs into trophoblasts and placental villi. **A** Confocal images of trophoblasts exposed to CeO_2 NPs coated with BaP: After 16 h of culture, VCT were treated for 48 h with CeO_2 NPs coated with 2 concentrations of BaP (Coating LR at 0.25 µM and Coating HR at 1 µM). After 48 h of treatment, trophoblasts were fixed and then immunolabeled with anti-E-cadherin (membrane marker, red) and anti-GATA3 (trophoblast marker, green) antibodies, and the nuclei were counterstained with Sytox Deep Red (magenta). Yellow arrows indicate aggregates. **B** and **C** Confocal images of placental villi and orthogonal views (volume and section) of 3D reconstructions of confocal images: Placental explants were pretreated or not for 1 h with 10 mM methyl-β cyclodextrin (MβCD) or 450 mM sucrose and then treated with 10 µg/cm^2 NPs coated with 1 µM BaP [Coating HR]. **(C)** As controls, placental explants were treated or not with 10 mM MβCD, 450 mM sucrose, cyclohexane solvent (CHX 0.25%), 1 µM BaP, and 10 µg/cm^2 CeO_2 NPs. After 48 h of treatment, placental explants were fixed and then immunolabeled with anti-cytokeratin7 (trophoblast marker, red) and anti-CD31 (endothelial marker, green) antibodies, and the nuclei were counterstained with Sytox Deep Red (magenta). *n* = 3 experiments. Scale bar: 10 µm

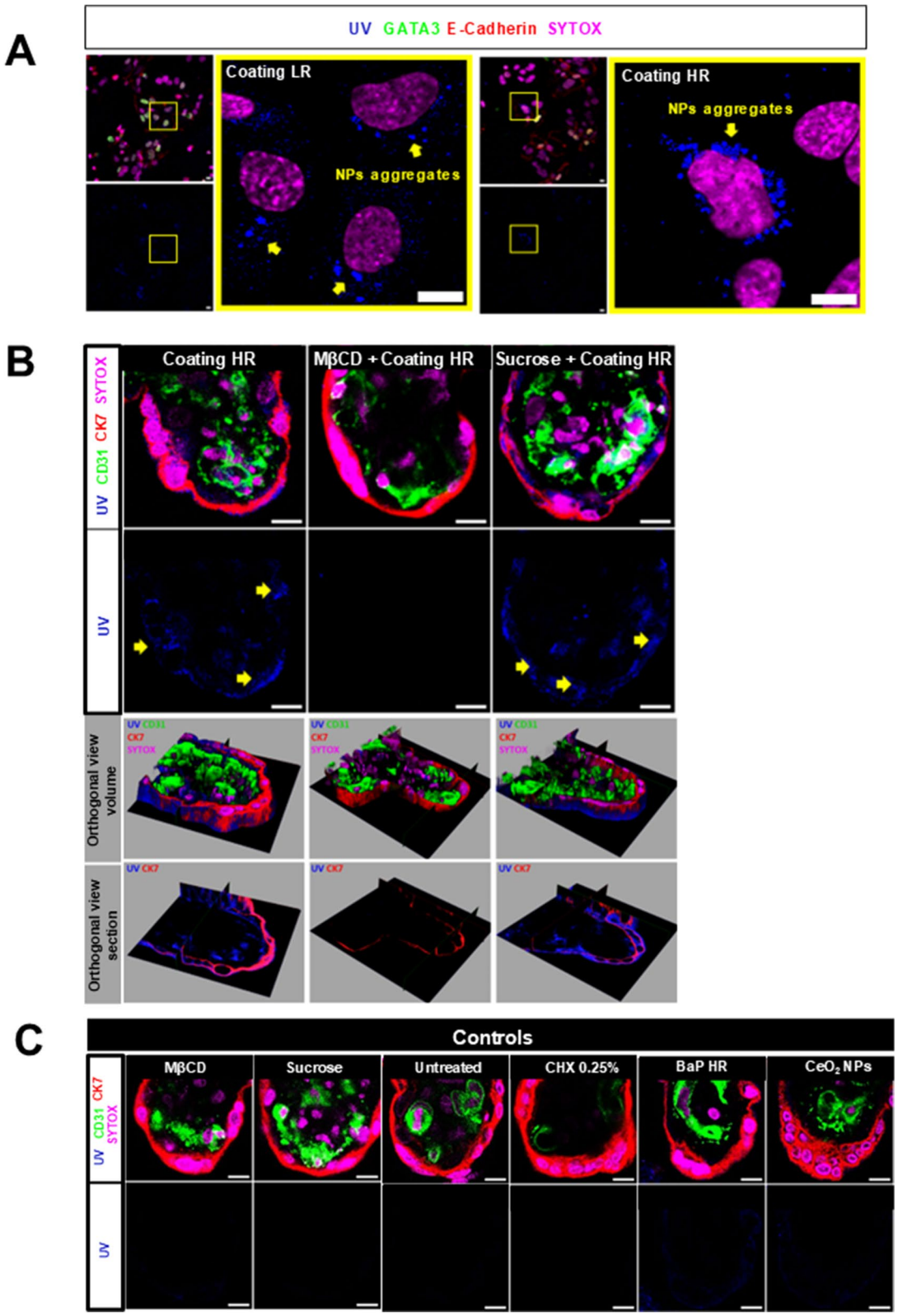

Fig. 10 (See legend on previous page.)

proteins) absorbed on the CeO_2 NPs, form a dynamic corona that can change over time and space. Indeed, NPs-coated molecules can be desorbed and replaced by other molecules with higher affinities depending on the cell environment [49]. As the protein corona can modify the physico-chemical characteristics of NPs [50] including their toxicity and their internalization capacity, the corona itself must be studied separately in a complementary study [51, 52]. Taken together, these findings support the deduction that surface-bound BaP remains bioavailable and may even potentiate AhR signaling.

Consequences for trophoblast differentiation

In this paper, we evaluated the impact of these pollutants alone and in mixtures on morphological differentiation capacity of trophoblasts: exposure to CeO_2 NPs impairs VCT differentiation into ST in agreement with our previous publication [21], while BaP alone or at low coating concentrations accelerates fusion, and co-exposure of NPs with BaP counterbalances their opposite effects, with differing impacts depending on BaP coating levels.

The negative effect of CeO_2 NPs on VCT fusion index could compromise the successful renewal of the syncytium throughout pregnancy and, thus, perturb placental function. This is underlined by the decrease in renewal capacity of ST that was associated with pregnancy disorders like preeclampsia or intrauterine growth restriction [53, 54]. We previously studied mechanisms involved in VCT fusion that could be affected by exposure to CeO_2 NPs, particularly the syncytin-1 and syncytin-2 proteins (with fusogenic properties), their receptors (ASCT2 and MFSD2, respectively), factors involved in VCT differentiation like GCM1 and in cell-to-cell adhesion CDH1, but we did not see any significant difference [21]. We can also hypothesize that CeO_2 NPs aggregates could mechanically prevent the trophoblast from moving, aggregating and finally fusing to form the ST. However, this was no longer the case when we used BaP-coated CeO_2 NPs, where the highest ratio (Coating HR) had no effect while the lowest ratio (Coating LR) had opposite effects and potentiat cell fusion.

The decrease in fusion index with an AhR antagonist suggests that BaP-induced trophoblastic differentiation is mediated through AhR activation, as confirmed by the reduced fusion rate when AhR was inhibited before exposure to low-ratio BaP-coated CeO_2 NPs, aligning with evidence that AhR influences both detoxification and cell differentiation [55–57]. AhR-knockout mice display impaired fertility, smaller litter size, and higher rates of neonatal mortality [58], indicating that AhR also plays an essential role during pregnancy [59]. These physiological roles of AhR can potentially switch when the placental barrier is exposed to pollutants such as BaP or BaP-coated CeO_2 NPs, to their detoxification, and in parallel. These pollutants may act as endocrine disruptors and, in our case, increase the fusion index of VCT. This is particularly relevant given the detection of BaP concentrations as high as 6.15 ng/g (0.02 µM) in dry weight placenta [60, 61], as well as the broader implication of placental PAH presence in pregnancy complications [62]. Thus, the balance between CeO_2-induced inhibition and BaP-induced acceleration of fusion appears to hinge on both BaP loading and its release kinetics.

Mitochondrial dynamics and functional adaptation

The study of mitochondrial phenotype revealed that CeO_2 NPs exposure elongates the mitochondrial network in VCT, likely due to their direct inhibitory effect on trophoblastic differentiation, which normally induces mitochondrial fragmentation and increases steroidogenic activity in ST [9]. Such elongation may serve as an adaptive mechanism in response to NP internalization and the activation of cellular processes such as autophagy [63], which has already been reported following exposure to CeO_2 NPs in a trophoblastic cell line [64, 65]. Indeed, elongated mitochondria can escape the macro-autophagy process and mitophagy [66] and are less susceptible to apoptosis [67]. It has already been demonstrated that CeO_2 NPs can impact the mitochondrial network and have a protective effect against apoptosis induction, preventing the fragmentation of the mitochondrial network (e.g. induced by Alzheimer's disease in neurons) [68]. This suggests an imbalance in mitochondrial dynamics, possibly reflecting a disruption of the fission–fusion cycle, which occurs constantly in the cell [9] with a complex machinery of dedicated proteins [6]. In the literature, it has been shown that during syncytialization of BeWo choriocarcinoma trophoblastic cells, protein levels of DRP-1 increase, and those of OPA1 and MFN1/2 decrease, leading to mitochondrial fragmentation in ST [6, 69]. Conversely, MFN1/2 and OPA1 levels are higher and DRP-1 levels are lower in VCT. Imbalance in mitochondrial dynamics (mitochondrial fusion/fission process) has been described for BaP metabolites, such as BPDE [70] and dioxin. Moreover, proteins of the mitochondrial dynamics machinery are affected in placental disorders such as preeclampsia [71]. We thus investigated the potential modification in the main players of mitochondrial dynamics after exposure to CeO_2 NPs, to which the mitochondrial network would respond by promoting network elongation through a decrease in mitochondrial fission and/or an increase in mitochondrial fusion. However, our study of mitochondrial dynamics in trophoblasts exposed to CeO_2 NPs showed no major

change in gene expression and protein levels of mitochondrial dynamics regulators (MFN1, MFN2 and OPA1 for fusion, DRP-1 and FIS-1 for fission and PGC-1α and VDAC1 for mitochondrial biogenesis).

In a previous publication, we showed that P4 secretion was maintained after exposure of trophoblasts to CeO_2 NPs [21], and here we found that ΔΨm was maintained, suggesting that elongated mitochondria could be an adaptation in order to maintain critical functions of mitochondrial functions and cell viability after exposure to CeO_2 NPs [6]. Conversely, treatment with BaP (coated on NPs or alone at the lower dose of 0.25 µM) decreased ΔΨm, in accordance with their higher ability to promote VCT differentiation into ST. As syncytium's energy production relies primarily on anaerobic metabolism, the atypical small mitochondria of ST have decreased ATP production, as compared to VCT, but a maintained ΔΨm, which is essential for cholesterol transport in mitochondria and for acquiring the steroidogenic activity of the syncytium, in particular for P4 production [8, 21]. Thus, our results may be due to the effect of BaP on cell differentiation, knowing that VCT have higher ΔΨm (which relies on mitochondrial oxidative phosphorylation for energy production) than ST (which are more steroidogenic and less ATP-producers) [69]. Therefore, we assessed the impact of BaP-coated CeO_2 NPs on mitochondrial respiration and found no significant impact overall. However, a decrease in basal respiration was noted for the co-exposure condition but not for individual exposure nor for exposure to BaP-coated CeO_2 NPs. Finally, to further investigate the impact of CeO_2 NPs on mitochondrial functions, we quantified steroid hormones and oxysterols produced by exposed VCTs. Indeed, steroid synthesis is initiated in the mitochondria of the syncytiotrophoblasts, while oxysterols, oxidized derivatives of cholesterol, have recently been shown to reduce trophoblast fusion [72]. Interestingly, the observed variations after CeO_2 NPs treatment were sex-specific. DHEA is converted to E2 and E1 by the action of placental P450 aromatase [73] and E1 is one of the major estrogens produced by the human placenta, alongside E2 and estriol (E3) [73]. Placental estrogens regulate several essential functions during pregnancy, such as maintaining fetal growth by influencing placental vascularization and metabolism, especially in uteroplacental vascular morphogenesis [74]. Although the overall increase in E1 after CeO_2 NPs exposure was modest (around 6%, reaching statistical significance because of the low SD), it coincided with a 25% reduction in its upstream precursor DHEA (Fig. 9A). This response was sex specific, the DHEA drop occurred only in male placentas, whereas E1 rise was confined to female placentas (Figure S6A). The placenta receives DHEA from both maternal adrenal glands and the fetal adrenals. Because VCTs lack P450c17 (CYP17A1) and cannot synthetize DHEA de novo, the DHEA detected in our trophoblasts culture must originate only from desulfation of DHEA-S present in the serum of the culture medium by placental steroid-sulfatase. The drop in trophoblasts DHEA therefore indicates either (i) CeO_2 NPs-mediated inhibition of steroid sulfatase activity and/or (ii) accelerated utilization of the limited DHEA pool for downstream reactions toward estrogens. The latter is consistent with the small but significant increase in E1, despite reduced precursors availability. Sex-dimorphic regulation offers an additional layer: male trophoblasts may express lower aromatase (CYP19A1) but exhibit higher steroid sulfonation capacity, rendering their intracellular DHEA pool more susceptible to depletion, whereas female trophoblasts may compensate by up-regulating aromatase and exporting newly synthetized estrogens. These complementary mechanisms can explain why the DHEA decrease is restricted to males and the slight E1 rise to females. It will be valuable, in a complementary study, to assess the expression and activity of key steroidogenic enzymes in relation to sex dimorphism following exposure to CeO_2 NPs. Functionally, reduced trophoblastic DHEA could limit the supply of neuro- and immuno-active steroids to male fetuses, potentially heightening their susceptibility to inflammatory stress, whereas the mild E1 elevation in females may promote angiogenesis and help counterbalance CeO_2 NP-induced placental stress.

The impact of CeO_2 NPs on trophoblastic mitochondria is therefore more complex than a simple negative effect on trophoblastic differentiation that would have uniformly decreased all hormones and increased mitochondrial respiration. Collectively, these results point to an adaptive elongation of the mitochondrial network that preserves ΔΨm and mitochondrial steroidogenesis despite NP-induced stress.

Internalization pathway of BaP-coated CeO_2 NPs

The results on CeO_2 NPs internalization from our previous publication [21] align with the existing literature. Chauhan et al. investigated the different internalization pathways (phagocytosis, pinocytosis and lipid raft-mediated uptake) in relation to CeO_2 nanostructures (NPs, nanorods and nanocubes) using a monocyte/macrophage cell line (RAW 264.7). The authors concluded that CeO_2 NPs are internalized via lipid rafts [41]. This raised the question of whether the same mechanism applies to placental chorionic villi exposed to CeO_2 NPs. We observed that both ratios of BaP-coated CeO_2 NPs are internalized in chorionic villi after exposure of the placental explants. Internalized BaP seems to be concentrated in local aggregates in a peri-nuclear area, as already reported by our

team for nude CeO_2 NPs [21]; thus, a part of BaP is probably still coated on CeO_2 NPs. We also showed a dose-dependent effect, with more abundant BaP aggregates signals for the higher ratio of BaP-coated CeO_2 NPs. This is in contradiction to the effects of the two ratios of BaP/CeO_2 NPs on VCT differentiation ability and AhR activation, where the lower dose had a higher effect. Thus, the effects of the lower ratio BaP/CeO_2 NPs on these two processes do not involve higher internalization capacity but rather higher bioavailability. Finally, our findings validated that BaP-coated CeO_2 NPs internalization in trophoblasts occurs through lipid raft-dependent pathways, consistent with Chauhan et al.'s observations for uncoated CeO_2 NPs [41], as demonstrated by selective inhibition with MβCD while other endocytosis inhibitors had no effect. The discrepancy between uptake level and biological effect underscores that bioavailability, rather than absolute intracellular load, is the critical determinant of AhR activation and differentiation outcome.

Conclusion

These findings have important clinical and exposomic implications, as they suggest that environmental pollutants like BaP, when complexed with CeO_2 NPs, can modulate key pathways involved in placental function, potentially influencing fetal development. The altered activation of AhR, disrupted trophoblast differentiation, mitochondrial homeostasis, and hormone secretion especially with sex-specific effects, highlight the need to consider nanoparticle-bound pollutants in exposome studies, as they may exhibit distinct bioavailability, persistence, and metabolic impacts compared to their free forms, ultimately affecting pregnancy outcomes and long-term health.

Abbreviations

A4	Androstenedione
AhR	Aryl hydrocarbon receptor
BaP	Benzo[a]pyrene
BPDE	Benzo[a]pyrene diol epoxide
CeO_2 NPs	Cerium dioxide nanoparticles
CHX	Cyclohexane
COX2	Cyclooxygenase 2
CTNNB	β-catenin
CV	Coefficient of variation
DHEA	Dehydroepiandrosterone
DHT	Dihydrotestosterone
DRP1	Dynamin-related protein 1
DSP	Desmoplakin
E1	Estrone
E2	Estradiol
ETC	Electron transport chain
FCS	Fetal calf serum
FCCP	Carbonyl cyanide-4 (trifluoromethoxy) phenylhydrazone
FIS1	Fission 1
GC-MS/MS	Gas chromatography-tandem mass spectrometry
GATA3	GATA binding protein 3
HBSS	Hanks' balanced salt solution
HR	High ratio
IARC	International agency for research on cancer
JC-1	5,5',6,6'-tetrachloro-1,1',3,3'-tetraethylbenzimidazolylcarbocyanine
LLOQ	Low limit of quantification
LR	Low ratio
Luc1.3	Firefly luciferase reporter gene
MFN1	Mitofusin 1
MFN2	Mitofusin 2
MβCD	Methyl-β-cyclodextrin
NPs	Nanoparticles
OPA1	Optic atrophy 1
OCR	Oxygen consumption rate
Oxysterols	- 7aOHC: 7α-hydroxycholesterol, - 7bOHC: 7β-hydroxycholesterol, - 25OHC: 25-hydroxycholesterol, - 7KChoL: 7-ketocholesterol, - 4bOHC: 4β-hydroxycholesterol
P4	Progesterone
PAH	Polycyclic aromatic hydrocarbons
PGC-1α	Peroxisome proliferator-activated receptor gamma coactivator 1-alpha
PM	Particulate matters
RPL13	Ribosomal protein L13
RPLP0	Ribosomal protein L0
SDHA	Succinate dehydrogenase complex flavoprotein subunit A
SEM	Standard error of the mean
ST	Syncytiotrophoblast
STED	Stimulated emission eepletion microscopy
Stau	Staurosporine
TCDD	Tetrachlorodibenzo-p-dioxin
TEM	Transmission electron microscopy
UFP	Ultrafine particles
VCT	Villous cytotrophoblasts
VDAC1	Voltage-dependent anion-selective channel 1
XME	Xenobiotic metabolizing enzymes
XRE	Xenobiotic response elements
ZrO_2 NPs	Zirconium dioxide nanoparticles

Supplementary Information

The online version contains supplementary material available at https://doi.org/10.1186/s12989-025-00640-x.

Supplementary Material 1: Table S1. Accuracy, target ions, corresponding deuterated internal control, detection range, low limit of quantification, and intra- and inter-assay CVs for steroid hormone quantification

Supplementary Material 2: Table S2. Accuracy, target ions, corresponding deuterated internal control, detection range, low limit of quantification, and intra- and inter-assay CVs for oxysterol quantification

Supplementary Material 3: Figure S1. Evaluation of the interference of CeO_2 NPs on luminescence readout. Measurements were performed on supernatants of NPs-treated cells before and after centrifugation or after addition of freshly prepared NPs to supernatants of cells not treated with NPs.

Supplementary Material 4: Figure S2. Evolution of the mitochondrial network during trophoblast differentiation. Thawed VCT were seeded and cultured in culture medium for 48 h. VCT were fixed and then immunolabeled with anti-COX2and nuclei were counterstained with Dapi. Representative confocal images of fixed VCT and syncytiotrophoblasts are shown

Supplementary Material 5: Figure S3. Effects of BaP-coated CeO_2 NPs on mitochondrial membrane potential of VCT treated for 24 h. After 16 h of culture, VCT were treated for 24 h with 10 µg/cm^2 CeO_2 NPs, 10 µg/cm^2 CeO_2 NPs coated with 2 concentrations of BaP, 10 µg/cm^2 CeO_2 NPs co-exposed with 2 concentrations of BaP, 2 concentrations of BaP alone, 2"vehicle"controls due to BaP dilution in cyclohexane, 3 µM of AhR antagonistor 1 µM staurosporineas positive depolarization control. After treatments, cells were incubated for 30 min at 37 °C with 1 µM of JC-1 dye. Representative images of fixed cells. In green, the monomeric form and in red, the aggregated form of JC-1 dye. Scale bar: 10 µm.Quantification of

membrane potentialcorresponding to the ratio of fluorescence intensities of the aggregated formto the monomeric form. Values are presented as the mean + SD of the normalized ratios to untreated cells. Statistical analysis was performed using one-way ANOVA againstuntreated control; * $p < 0.05$.

Supplementary Material 6: Figure S4. Loss of mitochondrial membrane potential during trophoblast differentiation. After 16 h of culture, VCT were treated for 24 h with 10 µg/cm^2 CeO_2 NPs, 10 µg/cm^2 CeO_2 NPs coated with 2 concentrations of BaP, 10 µg/cm^2 CeO_2 NPs co-exposed with 2 concentrations of BaP, 2 concentrations of BaP alone, 2"vehicle"controls due to BaP dilution in cyclohexane. After treatments, cells were incubated for 30 min at 37 °C with 1 µM of JC-1 dye. Cells were immunolabeled with an anti-E-cadherin membrane marker antibodyand nuclei were counterstained with DAPI. In green, the monomeric form and in red, the aggregated form of the JC-1 dye.Representative images of confocal acquisitions for each condition.Image magnification of the CHX solvent condition. ST demarcated in white dotted lines and VCT demarcated in yellow dotted lines. Scale bar: 10 µm.

Supplementary Material 7: Figure S5. Effects of BaP-coated CeO_2 NPs on oxygen consumption ratemeasured using Seahorse assay in VCT treated for 24 h. After 16 h of culture, VCT were treated for 48 h with 10 µg/cm^2 CeO_2 NPs, 10 µg/cm^2 CeO_2 NPs coated with 2 concentrations of BaP, 10 µg/cm^2 CeO_2 NPs co-exposed with 2 concentrations of BaP, 2 concentrations of BaP alone, solvent controls due to BaP dilution in cyclohexane, pre-treated or not with 3 µM AhR antagonistfor 1 h and then treated for 24 h with CeO_2 NPs coated with 0.25 µM BaP. To measure different oxygen consumption rateparameters, selective inhibitors were injected: oligomycin, carbonyl cyanide-4 phenylhydrazone, rotenone and antimycin A. The OCR values were normalized to the amount of DNA content from each well using Hoechst' stain. Three experimental conditions are shown: Control CHX and CeO_2 NPs, high ratioexposure, and low ratioexposure. OCR was measured over time following sequential injections of oligomycin, FCCP, and rotenone/antimycin A. The untreated condition is shown as a reference in all panels. Data are represented as mean ± SEM.

Supplementary Material 8: Figure S6. Effects of CeO_2 NPs on steroid and oxysterol production in VCT treated for 48 h according to placental sex. VCT purified from term placentas were plated overnight and were left untreated or incubated for 48 h with 10 µg/cm^2 CeO_2.The supernatants were collected, and the following steroid hormones were measured by GC–MS/MS: testosterone, estrone, estradiol, progesterone, 17-OH progesterone, dihydrotestosterone, dehydroepiandrosterone, 4-androstenedione.The following oxysterols were measured by GC–MS/MS: 7α-hydroxycholesterol, 7β-hydroxycholesterol, 5β,6β-epoxycholestanol, 25-hydroxycholesterol, 7-ketocholesterol, 4β-hydroxycholesterol. The hormone values were normalized to the protein content in the supernatants. Values are presented as mean ± SEM, regarding placental sex. Statistical analysis was performed using two-way ANOVA; * $p < 0.05$ versus Ctrl.

Supplementary Material 9: Figure S7. Excitation and emission spectra of benzo[a]pyrene. Excitation and emission spectra of benzo[a]pyrenewere obtained using a PerkinElmer LS 45 fluorescence spectrometer in a 1 cm^2 plastic cuvette at ambient temperature. BaP solution in cyclohexane that was kept away from light was diluted at 10 µM in placental culture medium. The emission spectrum of BaP was determined with an excitation at 370 nm.

Acknowledgements
The authors wish to thank the consenting patients, their babies and the clinical staff midwives of Diaconesses Croix Saint-Simon, Antony, and Montsouris Hospitals for providing placental tissues; as well as the Cellular and MOlecular Imaging Platform (PICMO), US25 Inserm, UAR3612 CNRS, Faculté de Pharmacie de Paris, Paris, France; Cell Imaging Platform, INSERM-US24-CNRS UMS 3633 Structure Fédérative de Recherche Necker, Université Paris Cité, Paris, France and CYTO2BM core facility of BioMedTech Facilities, INSERM US36, CNRS UAR 2009, Université Paris Cité for assistance with Seahorse analyses. We thank David Marsh for his careful English proofreading of the manuscript. This work was support by ANR (ANR-20-CE34-0003 PregNanoBaP) and by doctoral school BioSPC, Université Paris Cité, Paris, France.

Authors' contributions
Conceptualization: IF Data curation: IF, SD, GD Formal analysis: SD, GD, CM, MLV Funding acquisition: IF, TF Investigation: SD, GD, AT, FG, CM Methodology: SD, IF, AT, FG Project administration: IF Supervision: IF, MPGC, TF Validation: SD, GD, CM, AT, FG Visualization: SD, GD Writing – original draft: IF, GD Writing – review and editing: SD, GD, SB, CG, AT, FG, AZ, MPGC, XC, TF, IF.

Funding
This research was funded by ANR JCJC (PregNanoBaP, ANR-20-CE340003). G.D. was financed by the French Ministry of Research. This work was supported by the French National Institute of Health and Medical Research (INSERM) and by Université Paris Cité.
ANR JCJC,PregNanoBaP,ANR-20-CE340003,PregNanoBaP,ANR-20-CE340003,French Ministry of Research.

Data availability
No datasets were generated or analysed during the current study.

Declarations

Ethics approval and consent to participate
Placental samples were collected with patients' written informed consent at the maternity units of Diaconesses Croix Saint-Simon (75012 Paris, France), Antony Private Hospital (92160 Antony, France), and Institut Mutualiste Montsouris (75014 Paris, France). The study was conducted in accordance with the Declaration of Helsinki and approved by the local ethics committee (CPP 2015-mai-13909).

Consent for publication
Not applicable.

Competing interests
The authors declare no competing interests.

Author details
[1]Université Paris Cité, INSERM U1139, Fonctions Placentaires et Reproductives Microbiote pré et post-natal (FPRM), Faculté de Pharmacie, FHU Prem'IMPACT , Paris F-75006, France. [2]Inovarion, Paris F-75005, France. [3]Université Paris Cité, INSERM U1124, Health and Functional Exposomics - HealthFex, Paris F-75006, France. [4]AP-HP, Pôle Biologie-Pathologie Henri Mondor, INSERM U955, IMRB, Créteil F-94010, France. [5]Université Paris Cité, CNRS, Unité de Biologie Fonctionnelle et Adaptative, Paris 75013, France. [6]Université Paris-Saclay, Institut de Chimie des Substances Naturelles, CNRS UPR 2301, Gif-Sur-Yvette 91190, France.

Received: 5 July 2025 Accepted: 15 August 2025
Published online: 14 October 2025

References

1. Chatuphonprasert W, Jarukamjorn K, Ellinger I. Physiology and pathophysiology of steroid biosynthesis, transport and metabolism in the human placenta. Front Pharmacol. 2018;9: 1027.
2. Costa MA. The endocrine function of human placenta: an overview. Reprod Biomed Online. 2016;32(1):14–43.
3. Lecarpentier É, Vieillefosse S, Haddad B, Fournier T, Leguy MC, Guibourdenche J, et al. Placental growth factor (PlGF) and sFlt-1 during pregnancy: physiology, assay and interest in preeclampsia. Ann Biol Clin (Paris). 2016;74(3):259–67.
4. Tetro N, Moushaev S, Rubinchik-Stern M, Eyal S. The placental barrier: the gate and the fate in drug distribution. Pharm Res. 2018;35(4):71.
5. Giaginis C, Theocharis S, Tsantili-Kakoulidou A. Current toxicological aspects on drug and chemical transport and metabolism across the human placental barrier. Expert Opin Drug Metab Toxicol. 2012;8(10):1263–75.
6. Wasilewski M, Semenzato M, Rafelski SM, Robbins J, Bakardjiev AI, Scorrano L. Optic atrophy 1-dependent mitochondrial remodeling controls steroidogenesis in trophoblasts. Curr Biol. 2012;22(13):1228–34.

7. Martínez F, Kiriakidou M, Strauss JF 3rd. Structural and functional changes in mitochondria associated with trophoblast differentiation: methods to isolate enriched preparations of syncytiotrophoblast mitochondria. Endocrinology. 1997;138(5):2172–83.
8. De los Rios Castillo D, Zarco-Zavala M, Olvera-Sanchez S, Pardo JP, Juarez O, Martinez F, et al. Atypical cristae morphology of human syncytiotrophoblast mitochondria: role for complex V. J Biol Chem. 2011;286(27):23911–9.
9. Fisher JJ, Bartho LA, Perkins AV, Holland OJ. Placental mitochondria and reactive oxygen species in the physiology and pathophysiology of pregnancy. Clin Exp Pharmacol Physiol. 2020;47(1):176–84.
10. Cassee FR, van Balen EC, Singh C, Green D, Muijser H, Weinstein J, et al. Exposure, health and ecological effects review of engineered nanoscale cerium and cerium oxide associated with its use as a fuel additive. Crit Rev Toxicol. 2011;41(3):213–29.
11. Dale JG, Cox SS, Vance ME, Marr LC, Hochella MF Jr. Transformation of Cerium oxide nanoparticles from a diesel fuel additive during combustion in a diesel engine. Environ Sci Technol. 2017;51(4):1973–80.
12. Zhang JJ, Lee KB, He L, Seiffert J, Subramaniam P, Yang L, et al. Effects of a nanoceria fuel additive on the physicochemical properties of diesel exhaust particles. Environ Sci Process Impacts. 2016;18(10):1333–42.
13. Fajardie F, Verdier S, inventorsCigarette comprenant dans son filtre un catalyseur à base d'oxyde de cérium pour le traitement des fumées. France . 2002.
14. Kim SJ, Kim HC, Lee JH, inventorsSunscreen composition comprising surface-defected cerium oxide particles, and preparation method therefor. Korea. 2021.
15. Ma Y, Gao W, Zhang Z, Zhang S, Tian Z, Liu Y, et al. Regulating the surface of nanoceria and its applications in heterogeneous catalysis. Surf Sci Rep. 2018;73(1):1–36.
16. Aghebati-Maleki A, Dolati S, Ahmadi M, Baghbanzhadeh A, Asadi M, Fotouhi A, et al. Nanoparticles and cancer therapy: perspectives for application of nanoparticles in the treatment of cancers. J Cell Physiol. 2020;235(3):1962–72.
17. Wei J, Wang C, Yin S, Pi X, Jin L, Li Z, et al. Concentrations of rare earth elements in maternal serum during pregnancy and risk for fetal neural tube defects. Environ Int. 2020;137: 105542.
18. Zhang J, Nazarenko Y, Zhang L, Calderon L, Lee KB, Garfunkel E, et al. Impacts of a nanosized ceria additive on diesel engine emissions of particulate and gaseous pollutants. Environ Sci Technol. 2013;47(22):13077–85.
19. Wierzba W, Radowicki S, Bojar I, Pinkas J. Effects of environmental pollution with aromatic hydrocarbons on endocrine and metabolic functions of the human placenta. Ann Agric Environ Med. 2018;25(1):157–61.
20. Shadboorestan A, Koual M, Dairou J, Coumoul X. The role of the Kynurenine/AhR pathway in diseases related to metabolism and cancer. Int J Tryptophan Res. 2023;16: 11786469231185102.
21. Nedder M, Boland S, Devineau S, Zerrad-Saadi A, Rogozarski J, Lai-Kuen R, et al. Uptake of cerium dioxide nanoparticles and impact on viability, differentiation and functions of primary trophoblast cells from human placenta. Nanomaterials. 2020. https://doi.org/10.3390/nano10071309.
22. Deval G, Boland S, Fournier T, Ferecatu I. On placental toxicology studies and cerium dioxide nanoparticles. Int J Mol Sci. 2021;22(22): 12266.
23. Deval G, Nedder M, Degrelle S, Rogozarski J, Vignaud ML, Chissey A, et al. Benzo(a)pyrene and cerium dioxide nanoparticles in co-exposure impair human trophoblast cell stress signaling. Int J Mol Sci. 2023. https://doi.org/10.3390/ijms24065439.
24. Deval G, Mawas S, Devineau S, Borderie D, Mikolajczak C, Lefèvre G, et al. Effects of co-exposure to benzo-a-pyrene and cerium dioxide nanoparticles on human lung and placental barriers. Journal of Hazardous Materials Advances. 2025. https://doi.org/10.1016/j.hazadv.2025.100802.
25. Val S, Martinon L, Cachier H, Yahyaoui A, Marfaing H, Baeza-Squiban A. Role of size and composition of traffic and agricultural aerosols in the molecular responses triggered in airway epithelial cells. Inhal Toxicol. 2011;23(11):627–40.
26. Degrelle SA, Ferecatu I, Fournier T. Novel fluorescent and secreted transcriptional reporters for quantifying activity of the xenobiotic sensor aryl hydrocarbon receptor (AHR). Environ Int. 2022;169: 107545.
27. Alsat E, Mirlesse V, Fondacci C, Dodeur M, Evain-Brion D. Parathyroid hormone increases epidermal growth factor receptors in cultured human trophoblastic cells from early and term placenta. J Clin Endocrinol Metab. 1991;73(2):288–95.
28. Degrelle SA, Gerbaud P, Leconte L, Ferreira F, Pidoux G. Annexin-A5 organized in 2D-network at the plasmalemma eases human trophoblast fusion. Sci Rep. 2017;7: 42173.
29. Frendo JL, Cronier L, Bertin G, Guibourdenche J, Vidaud M, Evain-Brion D, et al. Involvement of connexin 43 in human trophoblast cell fusion and differentiation. J Cell Sci. 2003;116(Pt 16):3413–21.
30. Buchrieser J, Degrelle SA, Couderc T, Nevers Q, Disson O, Manet C, et al. *<IFITM* proteins inhibit placental syncytiotrophoblast formation and promote fetal demise. Science. 2019;365(6449):176–80.
31. Degrelle SA, Shoaito H, Fournier T. New Transcriptional Reporters to Quantify and Monitor PPARgamma Activity. PPAR Res. 2017;2017:6139107.
32. Shoaito H, Petit J, Chissey A, Auzeil N, Guibourdenche J, Gil S, et al. The role of peroxisome proliferator-activated receptor gamma (PPARgamma) in mono(2-ethylhexyl) phthalate (MEHP)-mediated cytotrophoblast differentiation. Environ Health Perspect. 2019;127(2):27003.
33. Shoaito H, Chauveau S, Gosseaume C, Bourguet W, Vigouroux C, Vatier C, et al. Peroxisome proliferator-activated receptor gamma-ligand-binding domain mutations associated with familial partial lipodystrophy type 3 disrupt human trophoblast fusion and fibroblast migration. J Cell Mol Med. 2020;24(13):7660–9.
34. Degrelle SA, Fournier T. Use of GATA3 and TWIST1 Immunofluorescence Staining to Assess In Vitro Syncytial Fusion Index. Methods Mol Biol. 2018;1710:165–71.
35. Agier V, Oliviero P, Lainé J, L'Hermitte-Stead C, Girard S, Fillaut S, et al. Defective mitochondrial fusion, altered respiratory function, and distorted cristae structure in skin fibroblasts with heterozygous OPA1 mutations. Biochimica et Biophysica Acta (BBA) - Molecular Basis of Disease. 2012;1822(10):1570–80.
36. Hemel I, Engelen BPH, Luber N, Gerards M. A hitchhiker's guide to mitochondrial quantification. Mitochondrion. 2021;59:216–24.
37. Chaudhry A, Shi R, Luciani DS. A pipeline for multidimensional confocal analysis of mitochondrial morphology, function, and dynamics in pancreatic β-cells. Am J Physiol Endocrinol Metab. 2020;318(2):E87-e101.
38. Pfaffl MW. A new mathematical model for relative quantification in real-time RT-PCR. Nucleic Acids Res. 2001;29(9): e45.
39. Giton F, Trabado S, Maione L, Sarfati J, Le Bouc Y, Brailly-Tabard S, et al. Sex steroids, precursors, and metabolite deficiencies in men with isolated hypogonadotropic hypogonadism and panhypopituitarism: a GCMS-based comparative study. J Clin Endocrinol Metab. 2015;100(2):E292–6.
40. Matos P, Horn JA, Beards F, Lui S, Desforges M, Harris LK. A role for the mitochondrial-associated protein p32 in regulation of trophoblast proliferation. Mol Hum Reprod. 2014;20(8):745–55.
41. Chauhan D, Sri S, Kumar R, Panda AK, Solanki PR. Evaluation of size, shape, and charge effect on the biological interaction and cellular uptake of cerium oxide nanostructures. Nanotechnology. 2021. https://doi.org/10.1088/1361-6528/ac03d5.
42. Martinez F, Milan R, Flores-Herrera O, Olvera-Sanchez S, Gomez-Chang E, Espinosa-Garcia M. The Role of Mitochondria in Syncytiotrophoblast Cells: Bioenergetics and Steroidogenesis. In: Zheng J, editor. Recent Advances in Research on the Human Placenta. Rijeka: IntechOpen; 2012.
43. Yang Y, Bao H, Chai Q, Wang Z, Sun Z, Fu C, et al. Toxicity, biodistribution and oxidative damage caused by zirconia nanoparticles after intravenous injection. Int J Nanomedicine. 2019;14:5175–86.
44. Lazić V, Pirković A, Sredojević D, Marković J, Papan J, Ahrenkiel SP, et al. Surface-modified ZrO2 nanoparticles with caffeic acid: characterization and in vitro evaluation of biosafety for placental cells. Chem Biol Interact. 2021;347: 109618.
45. Braun AE, Mitchel OR, Gonzalez TL, Sun T, Flowers AE, Pisarska MD, et al. Sex at the interface: the origin and impact of sex differences in the developing human placenta. Biol Sex Differ. 2022;13(1): 50.
46. Wakx A, Nedder M, Tomkiewicz-Raulet C, Dalmasso J, Chissey A, Boland S, et al. Expression, localization, and activity of the aryl hydrocarbon

receptor in the human placenta. Int J Mol Sci. 2018. https://doi.org/10.3390/ijms19123762.
47. Dmitrienko SG, Gurariy EY, Nosov RE, Zolotov YA. Solid-phase extraction of polycyclic aromatic hydrocarbons from aqueous samples using polyurethane foams in connection with solid-matrix spectrofluorimetry. Anal Lett. 2001;34(3):425–38.
48. Carriere M, Sauvaigo S, Douki T, Ravanat JL. Impact of nanoparticles on DNA repair processes: current knowledge and working hypotheses. Mutagenesis. 2017;32(1):203–13.
49. Canoa P, Simón-Vázquez R, Popplewell J, González-Fernández Á. A quantitative binding study of fibrinogen and human serum albumin to metal oxide nanoparticles by surface plasmon resonance. Biosens Bioelectron. 2015;74:376–83.
50. Ahsan SM, Rao CM, Ahmad MF. Nanoparticle-protein interaction: the significance and role of protein corona. Adv Exp Med Biol. 2018;1048:175–98.
51. Mishra RK, Ahmad A, Vyawahare A, Alam P, Khan TH, Khan R. Biological effects of formation of protein corona onto nanoparticles. Int J Biol Macromol. 2021;175:1–18.
52. Wang C, Chen B, He M, Hu B. Composition of intracellular protein corona around nanoparticles during internalization. ACS Nano. 2021;15(2):3108–22.
53. Roland CS, Hu J, Ren CE, Chen H, Li J, Varvoutis MS, et al. Morphological changes of placental syncytium and their implications for the pathogenesis of preeclampsia. Cell Mol Life Sci. 2016;73(2):365–76.
54. Huppertz B. The critical role of abnormal trophoblast development in the etiology of preeclampsia. Curr Pharm Biotechnol. 2018;19(10):771–80.
55. Safe S, Jin UH, Park H, Chapkin RS, Jayaraman A. Aryl hydrocarbon receptor (AHR) ligands as selective AHR modulators (SAHRMs). Int J Mol Sci. 2020. https://doi.org/10.3390/ijms21186654.
56. Larigot L, Benoit L, Koual M, Tomkiewicz C, Barouki R, Coumoul X. Aryl Hydrocarbon Receptor and Its Diverse Ligands and Functions: An Exposome Receptor. Annu Rev Pharmacol Toxicol. 2021.
57. Lin L, Dai Y, Xia Y. An overview of aryl hydrocarbon receptor ligands in the last two decades (2002–2022): a medicinal chemistry perspective. Eur J Med Chem. 2022;244: 114845.
58. Baba T, Mimura J, Nakamura N, Harada N, Yamamoto M, Morohashi K, et al. Intrinsic function of the aryl hydrocarbon (dioxin) receptor as a key factor in female reproduction. Mol Cell Biol. 2005;25(22):10040–51.
59. Stejskalova L, Pavek P. The function of cytochrome P450 1A1 enzyme (CYP1A1) and aryl hydrocarbon receptor (AhR) in the placenta. Curr Pharm Biotechnol. 2011;12(5):715–30.
60. Suter MA, Aagaard KM, Coarfa C, Robertson M, Zhou G, Jackson BP, et al. Association between elevated placental polycyclic aromatic hydrocarbons (PAHs) and PAH-DNA adducts from Superfund sites in Harris County, and increased risk of preterm birth (PTB). Biochem Biophys Res Commun. 2019;516(2):344–9.
61. Gladen BC, Zadorozhnaja TD, Chislovska N, Hryhorczuk DO, Kennicutt MC 2nd, Little RE. Polycyclic aromatic hydrocarbons in placenta. Hum Exp Toxicol. 2000;19(11):597–603.
62. Dong X, Wang Q, Peng J, Wu M, Pan B, Xing B. Transfer of polycyclic aromatic hydrocarbons from mother to fetus in relation to pregnancy complications. Sci Total Environ. 2018;636:61–8.
63. Gomes LC, Di Benedetto G, Scorrano L. During autophagy mitochondria elongate, are spared from degradation and sustain cell viability. Nat Cell Biol. 2011;13(5):589–98.
64. Chen Z, Geng Y, Gao R, Zhong H, Chen J, Mu X, et al. Maternal exposure to CeO(2)NPs derails placental development through trophoblast dysfunction mediated by excessive autophagy activation. J Nanobiotechnol. 2022;20(1): 131.
65. Yao M, Ji X, Zhang Y, Mao Z, Chi X. Mir-99 family is potential target to reverse cerium dioxide nanoparticle-induced placental cell dysfunction. Ann Transl Med. 2022;10(7):402.
66. Mundekkad D, Cho WC. Mitophagy induced by metal nanoparticles for cancer treatment. Pharmaceutics. 2022. https://doi.org/10.3390/pharmaceutics14112275.
67. Jeong SY, Seol DW. The role of mitochondria in apoptosis. BMB Rep. 2008;41(1):11–22.
68. Dowding JM, Song W, Bossy K, Karakoti A, Kumar A, Kim A, et al. Cerium oxide nanoparticles protect against Aβ-induced mitochondrial fragmentation and neuronal cell death. Cell Death Differ. 2014;21(10):1622–32.
69. Kolahi KS, Valent AM, Thornburg KL. Cytotrophoblast, not syncytiotrophoblast, dominates glycolysis and oxidative phosphorylation in human term placenta. Sci Rep. 2017;7:42941.
70. Wang W, Wang R, Zhang Q, Mor G, Zhang H. Benzo(a)pyren-7,8-dihydrodiol-9,10-epoxide induces human trophoblast Swan 71 cell dysfunctions due to cell apoptosis through disorder of mitochondrial fission/fusion. Environ Pollut. 2018;233:820–32.
71. Vishnyakova PA, Volodina MA, Tarasova NV, Marey MV, Tsvirkun DV, Vavina OV, et al. Mitochondrial role in adaptive response to stress conditions in preeclampsia. Sci Rep. 2016;6: 32410.
72. Aye IL, Waddell BJ, Mark PJ, Keelan JA. Oxysterols inhibit differentiation and fusion of term primary trophoblasts by activating liver X receptors. Placenta. 2011;32(2):183–91.
73. Evain-Brion D, Malassine A. Human placenta as an endocrine organ. Growth Horm IGF Res. 2003;13(Suppl A):S34–7.
74. Rusidzé M, Gargaros A, Fébrissy C, Dubucs C, Weyl A, Ousselin J, et al. Estrogen actions in placental vascular morphogenesis and spiral artery remodeling: a comparative view between humans and mice. Cells. 2023. https://doi.org/10.3390/cells12040620.

Publisher's Note